Quantum modeling of semiconductor gain materials and vertical-external-cavity surface-emitting laser systems

Feature Article

Christina Bückers[*,1], **Eckhard Kühn**[1], **Christoph Schlichenmaier**[1], **Sebastian Imhof**[2], **Angela Thränhardt**[2], **Jörg Hader**[3,4], **Jerome V. Moloney**[3,4], **Oleg Rubel**[5,6], **Wei Zhang**[7], **Thorsten Ackemann**[8], and **Stephan W. Koch**[1]

[1] Department of Physics and Material Sciences Center, Philipps-University Marburg, Renthof 5, 35032 Marburg, Germany
[2] Faculty of Natural Sciences, Chemnitz University of Technology, 09107 Chemnitz, Germany
[3] Nonlinear Control Strategies, Inc., 3542N. Geronimo Ave., Tucson, AZ 85705, USA
[4] College of Optical Sciences, University of Arizona, Tucson, AZ 85721, USA
[5] Thunder Bay Regional Research Institute, Thunder Bay, Canada ON P7A 7T1
[6] Department of Physics, Lakehead University, Thunder Bay, Canada ON P7B 5E1
[7] Centre for Biophotonics, SIPBS, University of Strathclyde, Glasgow G4 0NR, Scotland, UK
[8] SUPA and Department of Physics, University of Strathclyde, Glasgow G4 0NG, Scotland, UK

[*] Corresponding author: e-mail christina.bueckers@physik.uni-marburg.de, Fax: +49 6421 28 27076

This article gives an overview of the microscopic theory used to quantitatively model a wide range of semiconductor laser gain materials. As a snapshot of the current state of research, applications to a variety of actual quantum-well systems are presented. Detailed theory–experiment comparisons are shown and it is analyzed how the theory can be used to extract poorly known material parameters. The intrinsic laser loss processes due to radiative and nonradiative Auger recombination are evaluated microscopically. The results are used for realistic simulations of vertical-external-cavity surface-emitting laser systems. To account for nonequilibrium effects, a simplified model is presented using pre-computed microscopic scattering and dephasing rates. Prominent deviations from quasi-equilibrium carrier distributions are obtained under strong in-well pumping conditions.

1 Introduction The quantitative modeling of semiconductor laser materials and their electronic excitations is of significant importance for the design and development of efficient and optimized semiconductor laser devices. The accurate description of the important system ingredients is particularly critical in modern microlasers, where the properties of the relatively small amount of gain material has to be well adapted to the specific microcavity. Examples of current interest are vertical-external-cavity surface-emitting laser (VECSEL) systems also known as optically pumped semiconductor disk lasers, which have recently emerged as a new class of semiconductor lasers [1–5]. They combine the advantages of a semiconductor gain medium with the solid-state-laser cavity design and allow for the extraction of a high-power, diffraction-limited circular output beam [6, 7].

In the past decade, we have developed a many-particle theory to model the optical properties of semiconductor quantum-well structures which are the basic building blocks in common semiconductor lasers [8, 9]. By means of systematically derived microscopic equations, we quantitatively predict the absorption, gain, refractive index, luminescence, and the intrinsic laser losses of a system in a consistent way including microscopic interaction effects explicitly. The predictive capability of our model has been validated by experiments for various material systems with emission wavelengths from the ultraviolet and visible to the near- and mid-infrared (e.g., see Refs. [10–12]).

The microscopically calculated optical properties of semiconductor gain materials may be used to analyze and design laser devices. Especially, in microcavity lasers the proper description of the intricate interplay of the cavity and the optical response of the active layers is essential. Employing the microscopic approach, main characteristics of the laser device such as emission wavelength, threshold behavior, or input–output power characteristics can be evaluated.

This article reviews the application of the microscopic model to a wide range of material systems used in VECSEL and other laser systems. After our theoretical approach is briefly introduced (Section 2), we discuss some of the relevant properties of an (AlGaIn)As-based VECSEL system in Section 3. Emphasis is placed on the analysis of the lasing performance and in particular, the potential and limitations of optical in-well pumping are assessed. In Section 4, the laser gain and loss properties of the (AlGaInAs)(AsSb)-based material family are investigated and the application potential of various designs is explored. Section 5 addresses the characterization, the lasing properties, and disorder effects in the dilute nitride (GaIn)(NAs)-based material system. Furthermore, the suitability of our approach to extract critical structural parameters through the analysis of spectroscopic measurements is demonstrated in Section 6 for a Ga(AsSb)-based system. Finally, nonequilibrium effects are discussed in Section 7 highlighting the impact of the pumping concept on the performance of VECSEL systems.

2 Theoretical approach

Semiconductor laser devices are critically influenced by the optical response of the gain material so that any quantitative model requires a consistent quantum mechanical theory. For this purpose, we have developed a microscopic model enabling us to simulate the relevant electro-optical properties of semiconductor heterostructures in a consistent way. As the central part, the many-particle interactions are calculated explicitly. Only the structural layout and material constants are needed as input, and we do not have to resort to phenomenological parameters such as dephasing and scattering rates, linewidth enhancement factors, and the like.

The starting point of our approach is the calculation of the single-particle band structure and the corresponding Coulomb and dipole matrix elements. These are used as input for the microscopic determination of the absorption/gain, the photoluminescence, and the intrinsic laser loss processes. While absorption and photoluminescence investigations allow for an accurate characterization of semiconductor heterostructures, the laser gain and loss properties are relevant ingredients for the final performance of the laser device.

2.1 Band structure

For the computation of the single-particle eigenenergies and eigenstates in a semiconductor heterostructure, we apply $k \cdot p$-theory which is based on a perturbation method [13]. If we consider III–V semiconductors such as (AlGaIn)As- or (AlGaIn)(AsSb)-based materials, the eigenstates of the quantum well may be developed in split-off, heavy hole, light hole, and electronic contributions, each spin degenerated. In this manner, the band-structure information is contained in an 8×8 matrix, the so-called Luttinger matrix. However, for dilute nitride (GaIn)(NAs)-based structures the matrix has to be extended to a 10×10 matrix (Section 5). The required material parameters for the band structure calculation are taken from the literature [14, 15]. Finally, from the single-particle wavefunctions, we determine the optical dipole and Coulomb matrix elements needed for the microscopic computations.

2.2 Absorption and laser gain

In order to compute the absorption/gain, the semiconductor Bloch equations are solved in second Born–Markov approximation [16]. The equations describe the dynamics of the microscopic polarizations, i.e., the interband coherence at a certain momentum, which couple to carrier densities present in the system. In most of our applications, the carriers can be assumed to be in quasi-equilibrium and thus in a Fermi-Dirac distribution. However, the general approach also allows us to study the impact of nonequilibrium situations which are addressed in Section 7. Summing up the microscopic quantities yields the macroscopic polarization which gives the linear response of the material system to a light field.

In this manner, the refractive index change as well as the absorption/gain spectrum of a quantum well can be deduced. Since we calculate the many-particle correlations explicitly in second Born–Markov approximation, the homogeneous linewidth of the optical spectra is determined by quantum mechanical scattering equations including temperature, density, and spectral dependencies in a consistent way. Thus, phenomenological dephasing parameters are not required and unphysical features such as absorption below the band gap, wrong amplitudes, and incorrect line shapes are avoided [17]. Our microscopic approach has proven to realistically simulate the optical properties through many comparisons to experiments for a multitude of material systems (e.g., see Ref. [18]).

In laser systems such as VECSEL devices the semiconductor quantum wells are usually embedded in a microcavity. In order to take the dielectric environment into consideration, we employ the transfer matrix method which is a formalism accounting for the partial light reflectance and transmission through a structure containing several interfaces [19]. In the transfer matrix, we include the optical response of the active layers by adding the absorption/gain and the carrier-induced refractive index changes to the background refractive index of the quantum-well layers.

2.3 Photoluminescence

Spontaneous emission rates are calculated on the basis of the semiconductor luminescence equations [19], which include the equations of motion for the photon number in a given light mode and the photon-assisted polarizations. They have been derived similarly to the semiconductor Bloch equations, but involve

Feature

Article

Phys. Status Solidi B **247**, No. 4 (2010)   791

the quantization of the light field. As for the computation of the absorption/gain, it is essential to calculate the many-particle interactions explicitly since only the inclusion of the excitonic correlations ensures the correct line shape of the resulting luminescence spectrum of the quantum-well system.

If one wants to compare calculated and experimentally measured spectra of a VECSEL system, one has to take into account that the line shape of a photoluminescence spectrum detected at the surface of a VECSEL structure is modified by cavity effects. In order to account for the dielectric environment in such weak-coupling systems, we apply an approach based on the derivation of a filter function [20] which leads to the enhancement or reduction of the luminescence at certain wavelengths. If we multiply the filter function evaluated for the specific dielectric structure with the calculated emission spectrum of the isolated quantum well, we obtain the actually detected photoluminescence at the surface of the structure.

2.4 Laser loss processes The performance of a laser device is influenced not only by the gain but also by the losses in the system. The material loss processes are typically classified into carrier recombination at defect states, spontaneous emission, and Auger recombination. The individual contributions of the various processes depend on the particular material system and the operating conditions such as temperature and carrier density. Often, the defect losses are negligible if one is dealing with high-quality materials. Hence, one is left with the radiative and Auger losses which we calculate microscopically.

The radiative loss rate is deduced by integrating photoluminescence spectra which are obtained by solving the semiconductor luminescence equations. Furthermore, our microscopic approach allows for the computation of the nonradiative Auger recombination rates. For this purpose, we solve scattering equations for the electron and hole distribution functions [9], which are derived in the same formalism as the semiconductor Bloch and the semiconductor luminescence equations.

Phenomenologically, the spontaneous emission is expected to increase quadratically with the carrier density since two particles participate in the process. Auger scattering involves three particles, thus their contribution is supposed to increase cubically with carrier density. Although this might be a good approximation below transparency when the carriers basically obey Boltzmann statistics, we find strong deviations with increasing carrier density when phase-space filling effects become important [9]. Thus, especially in the density regime relevant for lasing in most VECSEL systems the phenomenological formulas fail. In contrast, the microscopic theory enables us to predict the radiative as well as the Auger losses quantitatively for any lasing condition [9, 21].

Altogether, the microscopic evaluation of both the laser gain and the losses, supplemented by heat conduction and cavity waveguiding calculations allows for a systematic analysis of semiconductor laser devices. Thus, the main characteristics of the system such as threshold behavior, gain saturation, or lasing wavelength can be studied and the potential of the specific designs can be explored.

3 (AlGaIn)As-based VECSEL systems Well-established active materials for laser applications are (AlGaIn)As compounds. This material system is widely used as a gain element in VECSEL devices. As a specific example, we focus here on a design for a VECSEL operating at a wavelength around 850 nm [22–24].

Conventionally, the active material is pumped optically by an external laser diode via barrier states from which the excited carriers relax into the quantum wells, thus generating the occupation inversion [25]. An attractive alternative could be the direct pumping of in-well states not only because this would reduce the excess energy (quantum defect) of the photogenerated carriers, but also since this technique enhances the wavelength range of possible pump sources, e.g., one could use bright and inexpensive diodes at 800–810 nm [26].

In order to characterize and identify the relevant ingredients determining the performance of the VECSEL device, we apply our systematic microscopic approach. To figure out design specifications of the structure, spectroscopic measurements are analyzed first.

3.1 Layout of the laser structure In a VECSEL device light is amplified by semiconductor quantum wells which are embedded in a cavity built of a Bragg reflector and an external outcoupling mirror which is aligned at a certain distance from the gain element. Here, we focus on a VECSEL structure intended to operate at an emission wavelength around 850 nm.

The Bragg reflector is grown on a GaAs wafer using 30 repeats of alternating AlAs and $(Al_{0.18}Ga_{0.82})As$ layers which differ in their refractive indices as can be seen in the profile (Fig. 1, top). Each layer of the stack is designed to have the same optical thickness. Hence, a high-reflectivity stop-band centered at a wavelength of about 836 nm with a width of about 84 nm for normal incidence is established. On top of the Bragg reflector the active region is deposited. It contains 17 $(Al_{0.115}Ga_{0.785}In_{0.10})As$ quantum wells which are 10 nm wide and are surrounded by barrier layers made of $(Al_{0.26}Ga_{0.74})As$. The quantum wells are arranged to coincidence with the antinodes of the standing wave pattern of the laser mode (Fig. 1, bottom). Due to the huge spatial overlap of the active layers with the light field maximal gain can be extracted. In between quantum wells and barrier layers the sample contains $(Al_{0.115}Ga_{0.785}In_{0.10})(As_{0.82}P_{0.18})$ layers to reduce strain effects which are caused by the different lattice constant of the quantum-well material compared to the other layers of the structure. However, the band gap of the quinternary material is almost equal to that of the barrier layer, thus in the microscopic calculations we assume the quantum wells to be sandwiched between $(Al_{0.26}Ga_{0.74})As$ for simplicity. Finally, an $(Al_{0.50}Ga_{0.50})As$
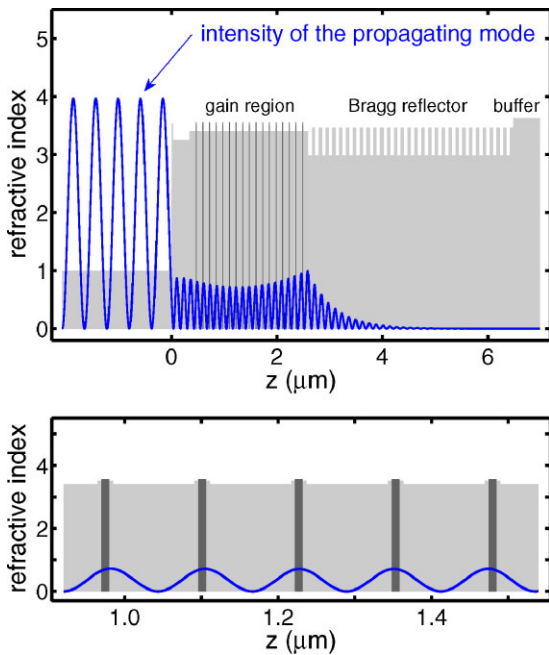
Figure 1 (online color at: www.pss-b.com) Top: Refractive index profile of the VECSEL structure at a temperature of 300 K (shaded area). The nominal structure consists of a resonant periodic gain region with 17 compressively strained $(Al_{0.115}Ga_{0.785}In_{0.10})As$ quantum wells embedded in $(Al_{0.26}Ga_{0.74})As$ barriers grown on a 30-pair $AlAs/(Al_{0.18}Ga_{0.82})As$ Bragg reflector. The quantum-well positions are indicated in darker gray. The curve represents the intensity of the light field at a wavelength of 850 nm along the structure. Bottom: Refractive index profile and intensity distribution of the laser mode within the resonant periodic gain structure.

Figure 2 (online color at: www.pss-b.com) Comparison of calculated (solid line) and measured (dashed line) reflectance spectrum of the VECSEL structure for normal incidence at a temperature of 300 K. In the simulation microscopically calculated low-density absorption spectra for the $(Al_{0.108}Ga_{0.785}In_{0.107})As/$ $(Al_{0.26}Ga_{0.74})As$ quantum wells are included. If the optical response of the quantum wells to the light field is not taken into account, the dash-dotted line will be obtained.

window layer and a $Ga(As_{0.90}P_{0.10})$ protective capping layer close the structure. Further details on design and growth of the sample are given in Ref. [23].

All these different components in the structure lead to steps in the refractive index profile which substantially affect the optical properties of the VECSEL. In particular, the large jump of the refractive index from air to the front surface of the sample shows much higher reflectance than the semiconductor interfaces within the sample. Thus, a subcavity is formed between the sample surface and the front of the Bragg reflector. The resonant periodic gain structure defines a laser mode with a wavelength of about 850 nm; however, this mode is not in resonance with the subcavity in the situation depicted in Fig. 1 because the mode exhibits a node at the front surface of the sample reducing the light coupling into the structure.

3.2 Optical characterization The analysis of spectroscopic measurements by the microscopic theory allows for a detailed characterization of the VECSEL structure. For this purpose, reflectance as well as photoluminescence investigations are carried out before building the laser cavity by aligning the external outcoupling mirror.
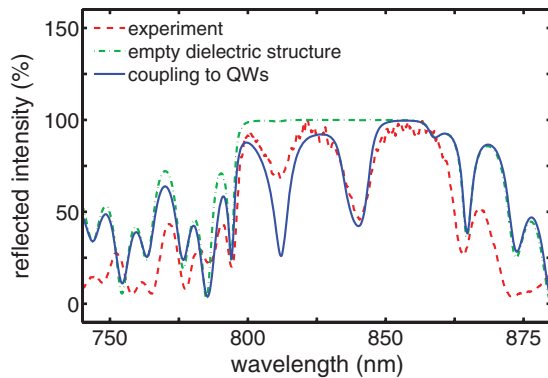
The reflectance spectrum of the sample measured at room temperature for normal incidence is plotted in Fig. 2 (dashed line). It is a result of interference effects of the light propagating and counter-propagating through the sample. In order to compute the reflectance and transmission at the boundaries of the dielectric structure, we employ the transfer matrix method. The required background refractive indices for the individual layers are extracted from the literature [14, 27, 28] also taking into account the index dispersion in the simulation. If we neglect the optical response of the quantum wells to the light field as a start, we find a flat high-reflectivity stop-band with adjacent interference features next to it (Fig. 2, dash-dotted line).

For a realistic description of the VECSEL structure it is crucial to include the active layers in the simulation. For this purpose, we pre-compute the wavelength-dependent optical susceptibility of the single quantum wells microscopically. The real part of the susceptibility determines the induced refractive index change in the quantum-well layer and the imaginary part gives the absorption with its characteristic excitonic peaks. These spectra represent a critical input to the VECSEL design and are obtained by solving the semiconductor Bloch equations for an $(Al_{0.108}Ga_{0.785}In_{0.107})As/$ $(Al_{0.26}Ga_{0.74})As$ quantum well in the low-density regime. The spectra are convoluted with a Gaussian distribution with a full-width at half-maximum of 8 meV to account for the growth inhomogeneities. The incorporation of the microscopically computed spectra in the transfer matrix calculation via wavelength-dependent complex refractive indices leads to a specific reduction of the reflectance at wavelengths where the quantum-well material has absorption (Fig. 2, solid line). Due to the increase of intracavity losses in the excitonic resonances, two pronounced absorption dips arise in the stop-band at 812 and 840 nm which match the experimental observation (Fig. 2, dashed line). The 840 nm

Phys. Status Solidi B **247**, No. 4 (2010)

Feature

Article

793

dip is caused by the subcavity resonance coinciding with the excitonic resonance induced by interband transitions between the first electron and the first hole subband.

The deviations of calculated and measured spectra outside the stop-band may be attributed to slight uncertainties of the parameters assumed for the layer widths and the refractive indices. As the structure consists of more than 130 layers, small changes of the individual structural parameters significantly affect the resulting reflectance, in particular regarding the side slopes of the spectrum. However, the spectral range outside the stop-band is not relevant for our current studies and thus no optimization attempts have been made.

As another independent method to characterize the VECSEL structure, we investigate the photoluminescence from the surface of the sample. The solutions of the semiconductor luminescence equations are shown in Fig. 3 as dash-dotted line. The main peak at 840 nm arises due to transitions between the first electron and the first hole subband. Furthermore, there is a second signal at 812 nm corresponding to higher-order interband transitions. To account for the dielectric environment of the cavity we evaluate the filter function (Fig. 3, inset). The product of this filter function with the microscopically calculated photoluminescence of the isolated quantum well yields the surface emitted photoluminescence spectrum (Fig. 3, solid line). The comparison shows that the photoluminescence signals are more pronounced because of the spectral filtering. Both, the photoluminescence line shape as well as the spectral position agree well with the measurements (Fig. 3, dashed line).

3.3 Light amplification and laser loss properties As soon as the VECSEL is pumped optically by an external laser diode, electrons are excited in the

Figure 4 (online color at: www.pss-b.com) Top: Reflectance of the VECSEL structure predicted at a temperature of 300 K for five different pumping levels. The underlying microscopically calculated absorption spectra for the $(Al_{0.108}Ga_{0.785}In_{0.107})As/(Al_{0.26}Ga_{0.74})As$ quantum well are displayed in the inset for carrier densities of 0.002, 2, 3, 4, and 5×10^{12} cm^{-2} (from top to bottom). Bottom: Reflectance of the VECSEL structure predicted at a carrier density of 3.7×10^{12} cm^{-2} per quantum well for a temperature of 300 K (solid line), 325 K (dash-dotted line), and 350 K (dashed line). In the experiment, lasing at 850 nm has been observed.

semiconductor structure. They relax to lower energies and occupy states near the band edge of the quantum-well material where they alter the optical response.

The characteristic dependence of the absorption spectrum on the carrier density is depicted in the inset of Fig. 4 (top) for a single $(Al_{0.108}Ga_{0.785}In_{0.107})As/(Al_{0.26}Ga_{0.74})As$ quantum well at a temperature of 300 K. The low-density spectrum shows excitonic signatures which correspond to optically strong interband transitions. With increasing occupation the peaks bleach out and finally, the absorption becomes negative in a spectral range near the band gap of the quantum-well material and we enter the regime of optical gain.

The microscopic results enter the transfer matrix calculation yielding the light intensity actually reflected by the VECSEL structure (Fig. 4, top). As soon as material gain is provided at the position of the cavity resonance, a narrow peak arises at 843 nm superimposed on the stop-band. The peak is slightly red shifted relative to the absorption dip obtained for low pumping because the coupling strength to the adjacent cavity resonance is modified. Obviously, the
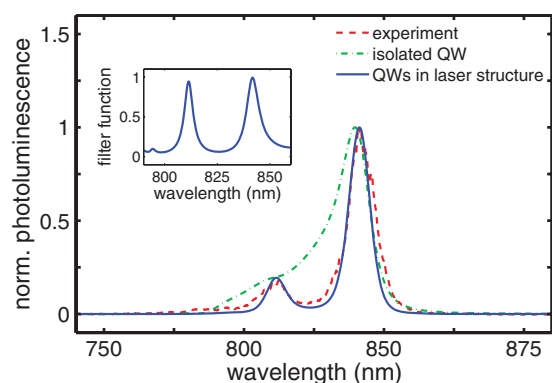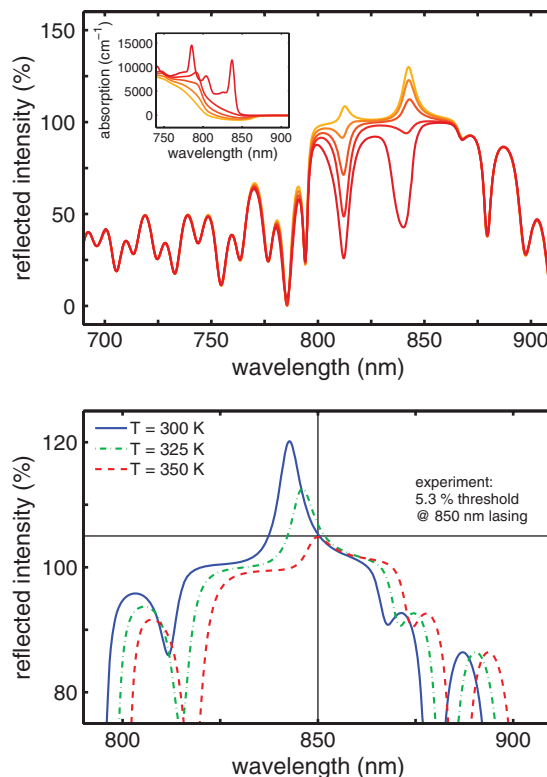

Figure 3 (online color at: www.pss-b.com) Comparison of calculated (solid line) and measured (dashed line) photoluminescence spectrum of the VECSEL structure for normal incidence at a temperature of 300 K. In the simulation cavity effects are taken into account by multiplying the microscopically calculated luminescence spectrum of the single $(Al_{0.108}Ga_{0.785}In_{0.107})As/(Al_{0.26}Ga_{0.74})As$ quantum well (dash-dotted line) with the wavelength-dependent filter function evaluated for the laser structure which is given in the inset.

reflectance becomes larger than 100%, i.e., the light intensity will be amplified by the system around the central wavelength. The amplification becomes more and more enhanced with increasing excitation due to the growth of the maximum of the underlying material gain spectra. However, a higher carrier density not only leads to a larger material gain, but also broadens the material gain spectrally. At a carrier density of $5 \times 10^{12}\,\mathrm{cm}^{-2}$ per quantum-well transparency is already exceeded for wavelengths around the next energetically higher cavity resonance so that a second region of light amplification occurs around 813 nm. However, with regard to laser operation only the central peak is relevant defining a lasing wavelength of 843 nm at room temperature because this is the wavelength favored by the resonant periodic gain structure.

Experimentally, laser operation is observed at about 850 nm. The red shift relative to the theoretically predicted lasing wavelength of 843 nm can be attributed to heating effects in the active region. With increasing temperature, the cavity resonance shifts to longer wavelengths by an amount of about 0.1 nm per Kelvin, and the spectral region providing material gain shifts even faster. If we carry out the calculations for a temperature of 350 K instead of 300 K, lasing at 850 nm is expected (Fig. 4, bottom). This value just matches the experimental finding. So we conclude a temperature increase of about 50 K in the active region which is a typical value for operating VECSEL devices reported in the literature [29].

The temperature increase results in a drop in amplification when the pumping power is kept constant. On the one hand, this trend is caused by the lower amplitude of material gain provided by the quantum wells as the carrier distribution smears out energetically with increasing temperature. On the other hand, with growing temperature the material gain shifts faster to longer wavelengths than the cavity resonance. For a temperature of 350 K the overlap of gain and cavity resonance is already strongly reduced. That is why one needs higher excitation densities to sustain a certain amplification level when the operating temperature increases. At 350 K we find a carrier density of $3.7 \times 10^{12}\,\mathrm{cm}^{-2}$ per quantum well required to achieve the lasing threshold of 5.3% gain. This value is mainly determined by the out-coupling losses, which are basically given by the reflectivity of the external mirror used to complete the laser cavity, and the internal losses of the laser.

From the engineering point of view, it is not only the carrier density which is important but also the pump intensity needed to sustain it. Hence it is crucial to study the loss processes in the semiconductor. Using our many-particle theory, the loss rate due to spontaneous emission and Auger recombination is evaluated for an $(Al_{0.108}Ga_{0.785}In_{0.107})As/(Al_{0.26}Ga_{0.74})As$ quantum well (Fig. 5). From the analysis we conclude that Auger processes play a minor role in this particular system compared to the radiative losses for the entire carrier density regime relevant for lasing. The recombination via defects is negligible. Since the VECSEL is expected to operate at about 350 K, the calculations are
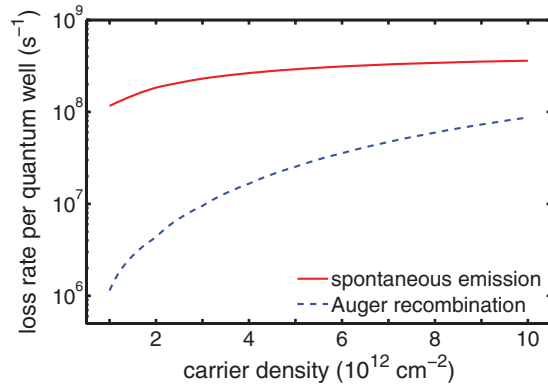

Figure 5 (online color at: www.pss-b.com) Laser losses due to spontaneous emission and Auger recombination as a function of the carrier density for an $(Al_{0.108}Ga_{0.785}In_{0.107})As/(Al_{0.26}Ga_{0.74})As$ quantum well at a temperature of 350 K.

carried out for this temperature. Compared to the results obtained at room temperature, the total loss rate is reduced by more than one order of magnitude. It is true, that the Auger rate increases with temperature, but more important for this material system are the radiative losses which become considerably lower because the probability of spontaneous emission is reduced due to the broadened carrier distributions for the higher temperature. However, the higher operating temperature also involves higher threshold carrier densities so that the benefits achieved by the reduced total laser losses are suspended.

3.4 Analysis of in-well pumping From the quantitative knowledge of the absorption, gain, and laser loss properties of the VECSEL structure the pump power necessary to achieve a certain amplification can be estimated by equating the carrier generation rate needed to sustain the gain against recombination. As discussed in Section 3.3, a carrier density of $3.7 \times 10^{12}\,\mathrm{cm}^{-2}$ per quantum well is identified to ensure an amplification of about 5.3% representing the threshold condition. For this threshold carrier density we find a loss rate of $2.7 \times 10^8\,\mathrm{s}^{-1}$ per quantum well which includes radiative as well as Auger recombination (see Fig. 5). As the loss rate has to be compensated by the pumping, we demand

$$N_{QW} R_{loss} n_{thr} = \frac{P_{pump}}{\hbar \omega_{pump}} \alpha(\omega_{pump}), \qquad (1)$$

where N_{QW} is the number of quantum wells, R_{loss} is the carrier loss rate per quantum well, n_{thr} is the threshold carrier density, P_{pump} is the pump power per pumped area, $\hbar \omega_{pump}$ is the energy of the pump light, and $\alpha(\omega_{pump})$ gives the fraction of the pump radiation absorbed through the structure. The latter can be extracted from the calculated reflectance and transmission spectra for the VECSEL structure and depends strongly on the pump wavelength (see Fig. 4).
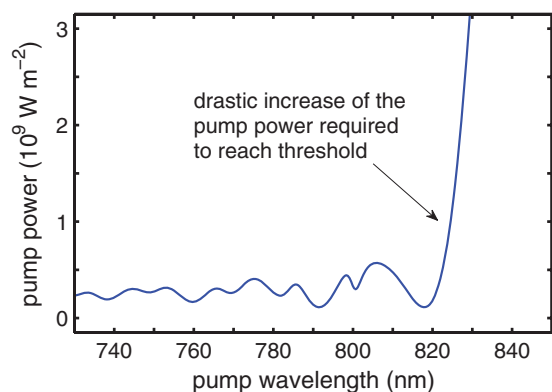
Phys. Status Solidi B **247**, No. 4 (2010)   795

Feature
Article

Figure 6 (online color at: www.pss-b.com) Pump power needed to sustain the threshold gain as a function of the pump wavelength. For the evaluation a temperature of 350 K is assumed in the active region.

In this manner, we estimate the threshold pump power as a function of the pump wavelength (Fig. 6). Obviously the efficiency of in-well pumping will drop rapidly if the pump wavelength is too close at the lasing wavelength. As soon as the pump wavelength exceeds a value of 822 nm, the required pump power increases drastically. In this spectral region the absorption is bleached out already by the induced generated carriers, thus limiting the pump wavelength.

The experimentally applied threshold pump intensity is 4.5×10^8 W m^{-2} for a pump wavelength between 806 and 810 nm. This corresponds quite well to the theoretical estimation. Differences could be caused by the fact that only parts of the pumped area contribute to lasing, thus the experimental threshold pump power per area might be larger. Moreover, in the calculation we assume each quantum well to be excited with equal power, but the absorption of the pump radiation might be rather inhomogeneous due to the fact that the standing wave distribution of the pump does not equal that of the laser and hence its antinodes are not optimally overlapping with the quantum wells.

It is worth noting that it is essential for the analysis to have the microscopic model allowing for quantitative predictions of the optical properties of the gain element in the VECSEL device. Simpler models would lead to incorrect conclusions as the lasing performance depends substantially on the spectral position of the quantum-well absorption/gain, its amplitude, the line shape of the spectra, as well as the temperature and carrier density of all these quantities. And besides, if the extracted threshold carrier density was incorrect, the error would be even further enhanced in the determination of the laser loss processes which react very sensitively to the assumed carrier density. The many-particle approach has proven to simulate all these aspects realistically, thus allowing for an accurate characterization. Hence, in particular the potential and limitations of optical in-well pumping for the 850 nm VECSEL could be analyzed with special emphasis on the bleaching of the pump absorption. One important consequence is that pump and lasing wavelength should be separated in this system by at least

25 nm to sustain the necessary threshold gain. This means, that 800–810 nm diodes can pump the 850 nm laser system quite efficiently.

It is interesting to investigate whether other material systems and wavelength regions can benefit from in-well pumping. For example, deep-blue and ultraviolet GaN diodes might be used to pump blue-green VECSELs and 670 nm diodes to drive VECSELs in the 700–750 nm region. Obviously, a microscopic theory as developed here will be very helpful in assessing these situations.

4 (AlGaIn)(AsSb)-based lasers for long wavelengths Semiconductor lasers emitting around 2 μm are of considerable interest for a multitude of applications such as medical diagnostics, material processing, or spectroscopic trace gas detection. Based on the (AlGaIn)(AsSb) material class various designs with emission wavelength from 1.8 up to 3 μm have been presented, including diode lasers as well as VECSEL devices [30–35].

In order to study the basic optical properties of a possible material system in the long-wavelength regime, we analyze the absorption/gain of a (GaIn)Sb quantum-well structure emitting around 2 μm by means of our microscopic approach. Here, we use our quantitative theory to deduce experimentally not directly obtainable quantities, in particular band-structure details. Besides the laser gain, also the laser loss processes are studied with the goal to explore the potential of different laser designs.

For emission wavelengths above 3 μm most conventional type-I quantum-well structures are not useful any more since high internal losses hamper their operation. An alternative concept to overcome these limitations are type-II "W" active regions [36]. Again, the physical processes affecting the lasing parameters of such a device can be analyzed by our microscopic approach.

4.1 Analysis of the laser gain properties For the wavelength regime around 2 μm quantum-well lasers employing ternary (GaIn)Sb compounds are well suited. Based on the microscopic theory we analyze the material properties, in particular the optical gain, of such a (GaIn)Sb laser structure [12].

The GaSb-based diode laser we consider contains three 10 nm wide compressively strained (Ga$_{0.78}$In$_{0.22}$)Sb quantum wells which are separated by (Al$_{0.30}$Ga$_{0.70}$)(As$_{0.02}$Sb$_{0.98}$) barriers with a thickness of 20 nm. The active region is surrounded by 400 nm wide layers on each side, also made of (Al$_{0.30}$Ga$_{0.70}$)(As$_{0.02}$Sb$_{0.98}$). These, in turn, are embedded in (Al$_{0.84}$Ga$_{0.16}$)(As$_{0.06}$Sb$_{0.94}$) cladding layers. As the cladding layers have a considerably lower refractive index according to the higher aluminum concentration there is a remarkable jump of the refractive index from the barrier to the cladding layer on each side and thus, an optical waveguide is formed enclosing the laser mode in between. The overlap of the optical mode with the active layers, i.e.,
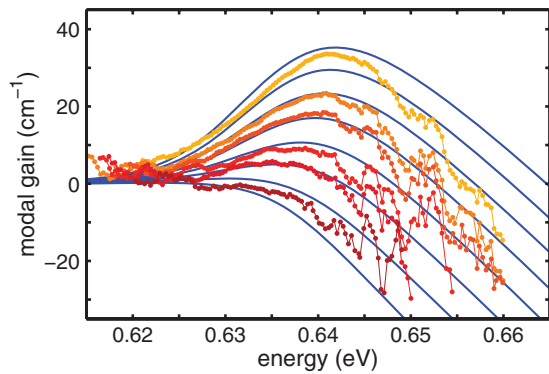
Figure 7 (online color at: www.pss-b.com) Comparison of calculated (solid lines) and measured (circles) modal gain spectra in the $(Ga_{0.78}In_{0.22})Sb/(Al_{0.30}Ga_{0.70})(As_{0.02}Sb_{0.98})$ laser structure at a temperature of 280 K for various excitations. In the simulation carrier densities of 0.65, 0.7, 0.75, 0.8, 0.85, 0.9, 0.95, and $1.0 \times 10^{12} \, cm^{-2}$ (from bottom to top) are assumed. The spectra are shifted 4 meV toward higher energies which can be attributed to slight deviations of the actual growth from the nominal design. The experimental spectra are obtained employing the method of Hakki and Paoli for excitation currents of 12.7, 14.6, 16.9, 18.9, 20.8, and 22.8 mA (from bottom to top). The experiment was done by M. Rattunde, N. Schulz, and J. Wagner at the "Fraunhofer Institut für Angewandte Festkörperphysik" [12].

the three quantum wells of the system, determines a confinement factor for the laser structure of about 6.6%. Actually, the amplification of the light mode through the system is given by the product of the confinement factor and the material gain provided by a single quantum well.

In order to study and analyze the gain properties of the laser structure, material gain spectra are computed based on the semiconductor Bloch equations for various carrier densities assuming a disorder-induced inhomogeneous broadening of 10 meV. Multiplying these spectra with the confinement factor yields the modal gain of the laser structure (Fig. 7, solid lines). In this manner, the calculations can be compared to experimental spectra. Here, we use gain for a 500 μm long and 6 μm wide ridge waveguide laser at various excitation currents below threshold employing the method of Hakki and Paoli (Fig. 7, circles). With growing excitation, the spectral width and amplitude increase as well as the gain maximum becomes slightly blue shifted. The spectral position of the gain peak matches within growth uncertainties and the line shape is also well reproduced.

The gain provided by the material system has a remarkably large amplitude exceeding that of more common GaAs-based structures. For illustration, in Fig. 8 (top) material gain spectra of the $(Ga_{0.78}In_{0.22})Sb$ quantum well are shown and compared to spectra obtained for the $(Al_{0.108}Ga_{0.785}In_{0.107})As$ quantum well employed in the VECSEL addressed in Section 3. Since the calculation assumes the same temperature and equal carrier densities in both cases, one clearly observes that the gain amplitude is considerably higher in the (GaIn)Sb structure. The maximal
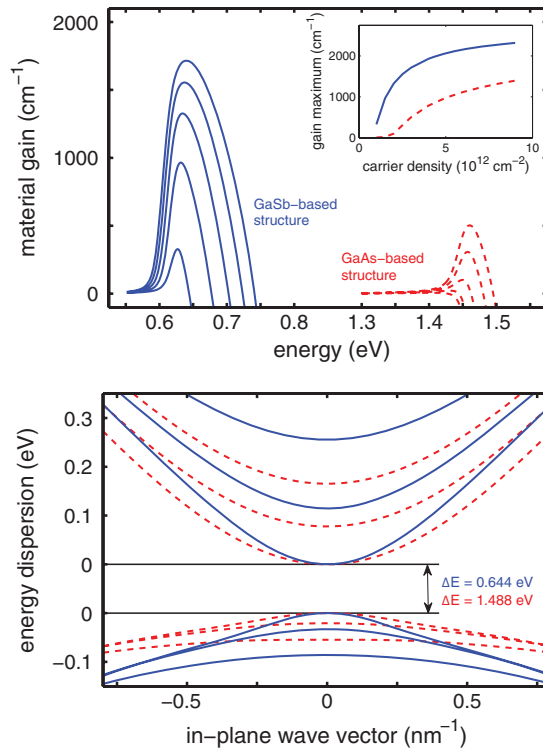

Figure 8 (online color at: www.pss-b.com) Top: Material gain spectra calculated for a $(Ga_{0.78}In_{0.22})Sb/(Al_{0.30}Ga_{0.70})(As_{0.02}Sb_{0.98})$ quantum well (solid lines) and an $(Al_{0.108}Ga_{0.785}In_{0.107})As/(Al_{0.26}Ga_{0.74})As$ quantum well (dashed lines) at a temperature of 300 K. Carrier densities of 1.0, 1.5, 2.0, 2.5, and $3.0 \times 10^{12} \, cm^{-2}$ (from bottom to top) are assumed. The inset depicts the maximum of the material gain as a function of the carrier density for both material systems. Bottom: Underlying band structure calculated for the $(Ga_{0.78}In_{0.22})Sb/(Al_{0.30}Ga_{0.70})(As_{0.02}Sb_{0.98})$ quantum well (solid lines) and the $(Al_{0.108}Ga_{0.785}In_{0.107})As/(Al_{0.26}Ga_{0.74})As$ quantum well (dashed lines). In order to compare the dispersion of the subbands in the two considered systems, the effective band gap ΔE is shifted to matching values in the figure. ΔE is 0.644 eV for the $(Ga_{0.78}In_{0.22})Sb$ and 1.488 eV for the $(Al_{0.108}Ga_{0.785}In_{0.107})As$ quantum well.

material gain which can be extracted is almost twice the value obtained for the GaAs-based structure (Fig. 8, top, inset).

The physical reasons for the beneficial gain properties of the GaSb-based material class are found in band-structure effects which are analyzed through a detailed comparison with the results for the GaAs-based system. On the one hand, the reduced band gap of (GaIn)Sb involves an increased gain amplitude, which will be visible if one performs the calculations again taking the band gap energy of the GaAs-based structure artificially at the value of (GaIn)Sb. On the other hand, the high gain in the (GaIn)Sb system is a result of an advantageous band dispersion (Fig. 8, bottom). The subbands of the GaSb-based structure are curved more strongly with the result that the effective masses are smaller compared to those of the GaAs-based system and they are more similar to the hole masses. Since these features offer optimized conditions for a low transparency density and a

high differential gain, the (GaIn)Sb system is more beneficial than the GaAs-based structure with heavier and more differing electron and hole masses. Besides, the electron as well as the hole subbands are separated better in the (GaIn)Sb case, thus states in higher subbands are less occupied and the number of carriers in the states contributing to the lasing transition increases for a given carrier density and temperature. Consequently, the combination of these band-structure effects leads to the excellent gain properties of the (GaIn)Sb material system.

4.2 Laser gain *versus* laser losses The high-gain amplitudes provided by the (AlGaIn)(AsSb) material class are advantageous of course to construct a laser. However, one also has to keep in mind the laser loss processes. As the microscopic theory allows for quantitative predictions of both the gain and the losses, the tradeoff between them can be studied systematically in order to develop optimized designs for certain applications.

For illustration, we perform a detailed comparison of two different designs, each intended to have an emission wavelength of about $2\,\mu m$ at room temperature. While design A is a 10 nm wide $(Ga_{0.78}In_{0.22})Sb$ quantum well embedded in $(Al_{0.30}Ga_{0.70})Sb$ barriers, the quantum well of design B is 12 nm thick, has a slightly lower indium concentration of 20% and furthermore, the height of the barrier layers is reduced by employing $(Al_{0.25}Ga_{0.75})Sb$.

With these design specifications the material gain of both systems peaks at about 0.62 eV (Fig. 9, top). However, the gain amplitude predicted for design A exceeds the amplitude expected for design B if equal carrier densities are assumed in the calculations. This aspect can be attributed to the fact that the carriers are less confined in design B due to the wider quantum well and the lower barrier height, thus the optical strength of the lasing transition is reduced. Maximally, a gain of about $2400\,cm^{-1}$ in case of design A and of about $1800\,cm^{-1}$ in case of design B can be extracted (Fig. 9, top, inset). These limits correspond to a saturation of the gain with increasing carrier density since a second peak grows out in the spectrum originating from higher-order quantum-well transitions.

In fact, the laser gain provided by design A is higher for a given carrier density, but the laser losses will be reduced remarkable if design B is chosen. The results of the microscopically calculated loss current due to spontaneous emission and Auger recombination are given in Fig. 9 (bottom) for both designs in dependence of the carrier density present in the quantum well. The Auger losses are found to dominate the radiative losses in the entire carrier density regime relevant for lasing, even at the transparency carrier density (about $0.9 \times 10^{12}\,cm^{-2}$ for design A and $1.0 \times 10^{12}\,cm^{-2}$ for design B).

The radiative losses are slightly smaller for design B because the carriers are less confined in the quantum wells, thus reducing the probability of the spontaneous recombination of an electron–hole pair. But what is rather crucial is that the Auger processes in design B are suppressed by more than a factor of 2.
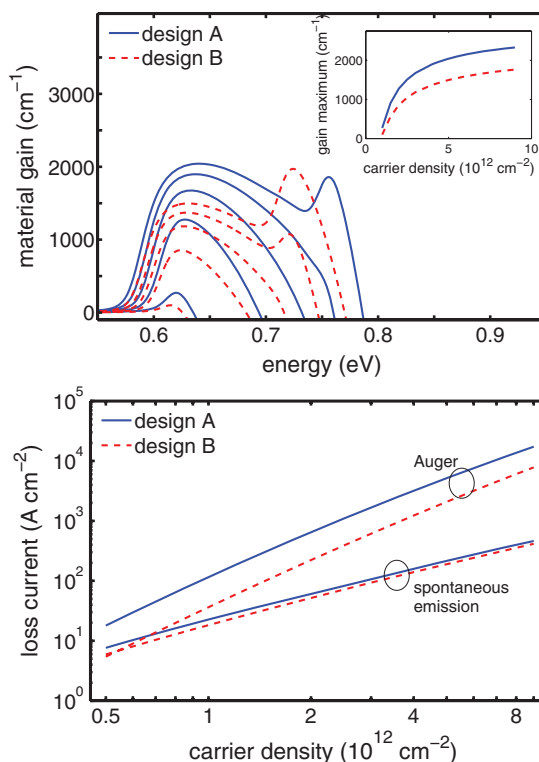

Figure 9 (online color at: www.pss-b.com) Top: Material gain spectra calculated for a 10 nm wide $(Ga_{0.78}In_{0.22})Sb/$ $(Al_{0.30}Ga_{0.70})Sb$ quantum well, denoted as design A (solid lines) and a 12 nm wide $(Ga_{0.80}In_{0.20})Sb/(Al_{0.25}Ga_{0.75})Sb$ quantum well, denoted as design B (dashed lines) at a temperature of 300 K. Carrier densities of 1, 2, 3, 4, and $5 \times 10^{12}\,cm^{-2}$ (from bottom to top) are assumed. The inset depicts the maximum of the material gain as a function of the carrier density for both material systems. Bottom: Laser loss current due to spontaneous emission and Auger recombination as a function of the carrier density for design A (solid lines) and design B (dashed lines) at a temperature of 300 K.

In order to assess the potential and limitations of the two proposed designs, we combine our quantitative knowledge about the laser gain and the laser loss properties. For this purpose, we extract the carrier density necessary to achieve a certain gain amplitude. Since this carrier density is connected to specific loss currents due to spontaneous emission and Auger recombination, we can evaluate the total loss current as a function of the material gain that is achieved (Fig. 10). To sustain the laser gain the total loss current has to be compensated by pumping the system, thus providing the appropriate number of carriers.

From the comparison we conclude that design A will be favorable, if one intends to achieve a laser gain of more than $1000\,cm^{-1}$ because under these conditions the required pump current is smaller than in case of design B where the laser characteristic is already affected by saturation effects of the gain. However, if one looks for a laser device with a low threshold current, design B will be much more advantageous. In fact, design B involves considerably lower pump currents, as long as gain amplitudes below $1000\,cm^{-1}$ are sufficient. If
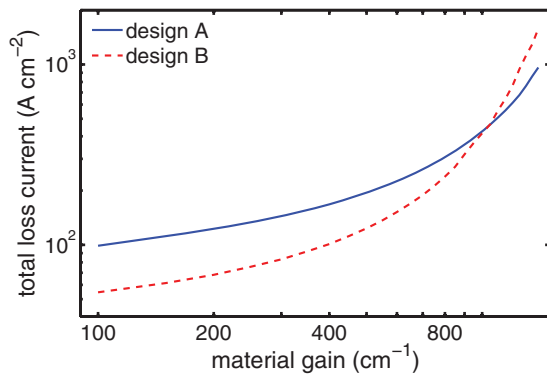
Figure 10 (online color at: www.pss-b.com) Laser loss current including radiative and Auger recombination as a function of the material gain provided for design A (solid line) and design B (dashed line) at a temperature of 300 K.
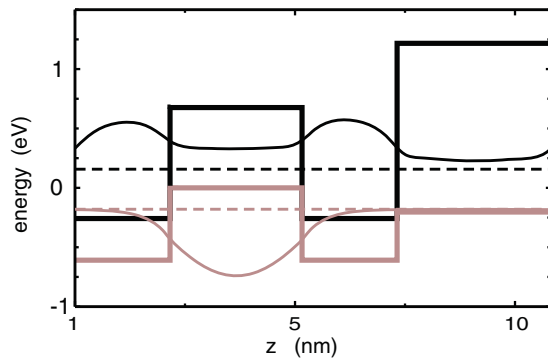

Figure 11 (online color at: www.pss-b.com) Confinement potential for electrons (black, thick line) and heavy holes (gray, thick line) in the "W" element of the laser structure, which is formed by a layer sequence of $InAs/(Ga_{0.925}In_{0.075})Sb/InAs/(Al_{0.53}Ga_{0.47})Sb$. The thinly plotted curves indicate the lowest electron and the lowest hole confinement wave function, respectively. The corresponding energy levels are marked as dashed lines.

we assume, for example, a threshold gain peak of $500\,cm^{-1}$, a threshold current of about $125\,A\,cm^{-2}$ has to be provided regarding design B. This amount is about 35% smaller than the pump current which has to be applied to design A to achieve the same gain amplitude.

It is worth noting that Auger losses are particularly strong in materials with narrow band gaps. Considering the (GaIn)Sb quantum well, the Auger processes dominate the spontaneous recombination even at transparency and they increase drastically with growing carrier density (Fig. 9, bottom). In contrast, in Section 3 we investigate for instance a GaAs-based $(Al_{0.108}Ga_{0.785}In_{0.107})As$ quantum-well structure which has a band gap that is twice as large as the band gap of (GaIn)Sb, and for this system the contribution of Auger recombination plays a minor role compared to the radiative losses (Fig. 5). Because of the particular high Auger losses in the GaSb-based material system adequate designs are required to overcome these limitations. The comparison of design A and design B demonstrates that the potential of various structural layouts can be studied systematically on the basis of the microscopic approach. In this manner, structures with, e.g., low threshold or high output power are found, so that laser devices can be optimized with regard to applications.

4.3 Investigation of mid-infrared type-II "W" diode lasers The quantum-well structures presented in Sections 4.1 and 4.2 are suitable for laser emission from 1.8 up to 3 μm. However, if one aims for even longer emission wavelengths in the mid-infrared, their operation will be strong affected by high internal losses. To circumvent these limitations alternative concepts have been considered, in particular diode lasers with type-II "W" active regions are discussed [36]. They fill the spectral range between 3 and 4 μm given by type-I quantum-well lasers on the short-wavelength side and by quantum-cascade lasers [37] on the long-wavelength side. Based on the microscopic theory, we investigate the lasing properties of an antimonide type-II "W" diode laser structure emitting at 3.4 μm [38].

The laser structure consists of five so-called "W" elements [39]. Each is formed by a 3 nm wide $(Ga_{0.925}In_{0.075})Sb$ hole quantum well which is sandwiched between 2.16 nm thick InAs layers providing wells for the electrons. These layers are in turn embedded in $(Al_{0.53}Ga_{0.47})Sb$. Thus, a short type-II superlattice is formed where electrons and holes are localized in adjacent layers (Fig. 11). Since electrons and holes are locally separated in the type-II structure, the Auger coupling strength is reduced so that the loss rate is smaller than in a type-I situation where electrons and holes are confined in the same layer. Obviously, the type-II design also involves reduced gain amplitudes, but what is rather crucial is the tradeoff between reduced losses and reduced gain.

By evaluating the laser gain and the laser losses microscopically, we predict the threshold current of the laser diode in a temperature range between 80 and 300 K. The results are in quantitative agreement with the experiment and a considerable increase of the threshold current with growing temperature is observed [38]. Through the microscopic analysis this behavior can be attributed to a thermally reduced gain amplitude which involves higher threshold carrier densities and thus higher-loss currents. In contrast, the Auger coefficient is found to be nearly temperature independent.

5 (GaIn)(NAs)-based material system After first reports of an increasing red shift of the band-edge luminescence with increasing nitrogen content in 1992 [40] (GaIn)(NAs) has been under intense investigation for its potential application as a GaAs-based laser material at telecommunication wavelengths. The most widely known specialty of (GaIn)(NAs) and related materials is the huge, composition-dependent bandgap bowing which also accounts for the unexpectedly small bandgap. The intricate band structure may be described by the anticrossing model

Phys. Status Solidi B **247**, No. 4 (2010)

Feature

Article

799

[41–43] where the nitrogen atoms are identified with an impurity band interfering with the conduction band. The resulting anticrossing pushes the conduction band edge to lower energies. In the formalism of $\boldsymbol{k} \cdot \boldsymbol{p}$-theory, the anticrossing model corresponds to an extension of the 8×8 to a 10×10 matrix.

5.1 Characterization of (GaIn)(NAs) structures

In order to use (GaIn)(NAs) material to its maximum potential, it has to be characterized thoroughly. However, being a long-wavelength material grown on GaAs, a number of characterization measurements are hampered by substrate absorption. Photomodulated reflectance [44–46] offers a possibility to sensitively measure optical spectra without substrate interference. This enabled a study of the type-I–type-II transition in a series of (InGa)As/Ga(N$_x$As$_{1-x}$) samples. Four samples with nitrogen contents $x = 0.48, 0.72, 1.25$, and 2.2% were investigated [47].

Photomodulated reflectance experiments are performed by varying a modulation pump between zero and a small value while measuring the change in reflectance with the help of a probe beam. The microscopic simulation of photomodulated reflectance is not straightforward because the mechanism causing the reflectance change is largely unknown. Our calculations were performed by determining the difference between two spectra at slightly varying densities. It is widely assumed that the modulation signal is caused by a change in electric field in the sample due to local charge inhomogeneities. We model these effects by solving Poisson's equation but find the signals dominated by the pump-induced density change rather than the electric field.

Figure 12 shows a calculated absorption spectrum (dashed line) for a series of three 9.4 nm wide (In$_{0.23}$Ga$_{0.77}$)As wells between 35 nm wide Ga(N$_{0.0048}$As$_{0.9952}$) barriers and the corresponding calculated photomodulated reflectance signal (solid line). For comparison, the experimental curve is also shown. Looking at the two theory curves for absorption and photomodulated reflectance, we remark that the peak
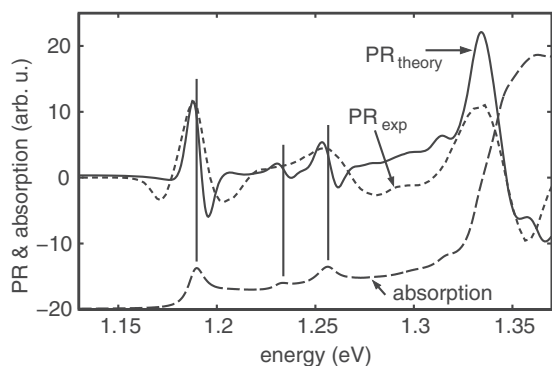

Figure 12 Calculated (solid line) and measured (dotted line) photomodulated reflectance spectra at a temperature of 300 K for a structure consisting of 9.4 nm wide (In$_{0.23}$Ga$_{0.77}$)As quantum wells between 35 nm wide Ga(N$_{0.0048}$As$_{0.9952}$) barriers. The calculated absorption spectrum (dashed line) is vertically displaced for clarity. Taken from Ref. [47].
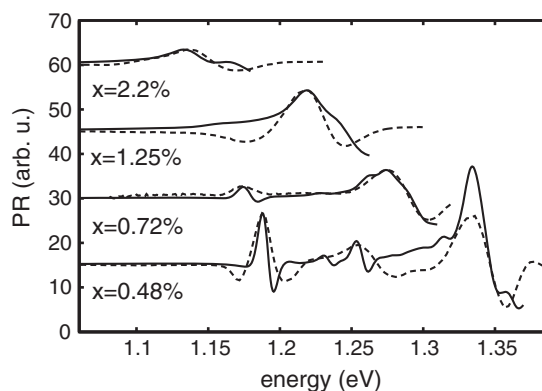

Figure 13 Calculated (solid lines) and measured (dashed lines) photomodulated reflectance spectra for the four samples investigated here. The nitrogen content in the barriers varies from $x = 0.48$, 0.72, 1.25, to 2.2%. A type-I–type-II transition can be shown to occur between $x = 0.72\%$ and $x = 1.25\%$. The spectra are vertically displaced for clarity. Taken from Ref. [47].

absorption energies are approximately given by the zero crossings of the differential signal. The calculation reproduces the main features of the experiment even without any line fitting parameters. The only adjustable quantity is the disorder-induced inhomogeneous broadening which was set to 6.7 meV to model the experiment.

Figure 13 extends the theory–experiment comparison to include four samples with different nitrogen contents in the barriers, $x = 0.48, 0.72, 1.25$, and 2.2%. For all cases, the main features are clearly reproduced. Some transitions are less pronounced in the experiment, probably due to sample inhomogeneities. Regarding the lowest transition, we see it move to lower energies and lose oscillator strength from $x = 0.48\%$ to $x = 0.72\%$ and attribute this effect to the decreasing electron confinement. For the $x = 1.25\%$ structure the transition has vanished as a result of the type-I–type-II transition with rising nitrogen content. In Ref. [47], this transition was further illustrated using a combination of experimental methods.

These spectra are an example of a wide range of experiments in (GaIn)(NAs) which can be modeled by microscopic theory. Further works in this area may be found in Refs. [8, 48, 49].

5.2 Toward 1.55 μm

In recent years, the growth of high-quality (GaIn)(NAs) material emitting at a wavelength of 1.55 μm has increasingly become attainable. Even though progress has been slow due to the high indium and nitrogen contents involved, relatively low threshold lasers beyond 1.55 μm have been demonstrated [50]. A major improvement in growth outcome may be achieved by the addition of antimony [51–55].

Our microscopic model allows us to consider the gain and loss properties of (GaIn)(NAs) in the entire 1.3–1.55 μm range independent of any growth issues [56], addressing the question whether the degrading of optical properties at higher wavelengths is an intrinsic- or a material-quality-
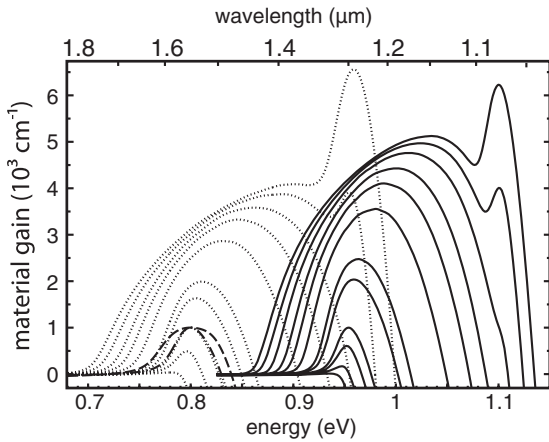
Figure 14 Intensity gain at 1.3 μm (solid lines) and 1.55 μm (dotted lines) for a quantum-well structure containing 40% indium. The dashed and dash-dotted lines show the effect of different strains which may be achieved by varying both indium and nitrogen contents, but keeping the emission wavelength constant. The dashed line corresponds to an unstrained sample. Obviously, the gain is much broader, and correspondingly the required carrier density is almost twice as high.

related phenomenon. Figure 14 shows the intensity gain at 1.3 μm (solid lines) and 1.55 μm (dotted lines) in a quantum-well structure containing 40% indium. The nitrogen content was varied from 0.55 to 2.3% in order to change the emission wavelength.

(GaIn)(NAs) being a quaternary material, different compositions may be used to achieve emission at a specific wavelength. Samples with different indium and nitrogen contents but emitting at the same wavelength are also compared in Fig. 14. The dashed and dash-dotted lines show the effect of different compositions at a constant emission wavelength of 1.3 μm. For instance, the dashed line corresponds to an unstrained sample. Obviously, the gain is much broader, and correspondingly the required carrier density is almost twice as high as for the 40% indium structure. To illustrate this dependence, we investigate two series of materials:

A *Constant indium*: The indium content is kept at 40%, the wavelength is varied by changing the nitrogen content.
B *Constant strain*: The strain is kept constant by varying both indium and nitrogen contents.

Figure 15 shows the carrier density necessary to obtain a certain peak gain for the two material series at 1.3 and 1.55 μm. As discussed before, the density is lower for the highly strained samples with 40% indium content ($e_{xx} = -2.65\%$ for 1.3 μm, $e_{xx} = -2.35\%$ for 1.55 μm). This is also visible in the inset which is a magnification of the large figure for small gains.

Having access to the full information in our microscopic calculation, we can explain the effects in detail. The
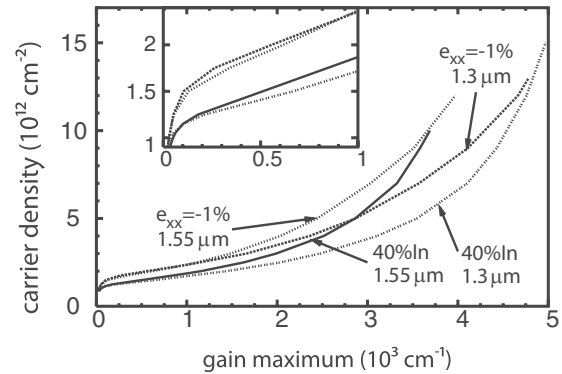

Figure 15 Carrier density necessary to obtain a certain peak gain for the two material series at 1.3 and 1.55 μm. Series A: 1.55 μm structure (solid) and 1.3 μm structure (dash-dotted). Series B: 1.55 μm structure (dotted) and 1.3 μm structure (dashed). The inset is a magnification of the large figure for small gains.

differences in required density are due to the band structure where composition changes induce the following effects:

1. Increased energetic separation of nitrogen level and conduction band edge for increased nitrogen content.
2. Decreased electron mass for reduced nitrogen content and increased indium content.
3. Splitoff of light holes due to compressive strain, higher strain raises the heavy hole content of the confined subbands and reduces their effective mass.

Comparing series A and B in the light of the above band structure dependencies, we remark that effect (2) and (3) lead to the observed higher gain for a given density for series A, while effect (1) weakens this phenomenon. In this quaternary material, one must thus strive to include as much strain as possible while still maintaining a high material quality.

Next, we microscopically calculate losses by Auger and spontaneous emission processes. Being a long-wavelength material, Auger processes clearly dominate [56]. In order to identify the gain region where the excitation of the quantum well is most efficiently turned into light amplification, we divide the total loss current $J_{tot} = J_{mono} + J_{sp} + J_{aug}$ by the peak gain. Here, J_{mono}, J_{sp}, and J_{aug} are loss currents by monomolecular, spontaneous, and Auger recombination, respectively. The monomolecular contribution is caused by nonradiative recombination processes at defect states and thus, basically depends on the quality of the material. The corresponding loss current is given by $J_{mono} = e\tau^{-1}\rho$, where e is the unit charge, $\tau = 1$ ns is a typical decay time in a (GaIn)(NAs) laser for 1300 nm emission [57], and ρ is the carrier density. The loss/current ratios show a clear minimum between 1000 and 2000 cm^{-1} which is thus the optimum operation range for a laser (Fig. 16).

In multi-quantum well structures, a reduction of losses can be achieved if the total number of quantum wells is adjusted such that the individual quantum wells operate in the optimum range. Pumping the quantum wells too hard,
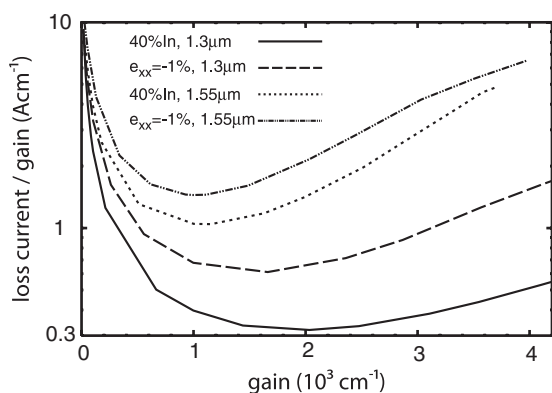
Phys. Status Solidi B **247**, No. 4 (2010)

801

Figure 16 Ratio of total loss current to peak gain. For the monomolecular loss, a monomolecular recombination time of 1 ns is assumed.

i.e., outside this regime, causes strong and dominant Auger losses. By contrast, close to the transparency point of the quantum well there are considerable monomolecular losses compared to a small gain.

5.3 Disorder in (GaIn)(NAs) So far, we included disorder effects only phenomenologically via inhomogeneous broadening. Even though this approach is appropriate for relatively homogeneous materials other systems, especially quaternaries may suffer from more serious disorder effects due to alloying and interfaces. For a thorough theoretical treatment of disorder, different regimes must be distinguished. At room temperature and especially in the high-density case discussed in Section 5.2, many-body effects rather than disorder dominate the signal. The opposite limit is the low-temperature, low-density regime where experimentally, strong disorder signatures are observed [58–62], in particular the so-called S-shape behavior of the photoluminescence energy and thus the Stokes shift. The effect consists of a nonmonotoneous temperature dependency, showing first a red shift, then a blue shift with rising temperature. The phenomenon is well known in other materials [63, 64] and can be modeled in the framework of hopping of bound excitons in a tail of localized states inherent to (GaIn)(NAs) [62, 65] by employing the kinetic Monte Carlo algorithm suggested in Ref. [66]. A simulation of excitons hopping in a manifold of localized states with the exponential energy distribution

$$g(\varepsilon_0) = \frac{N_0}{\varepsilon_0} \exp\left(\frac{\varepsilon}{\varepsilon_0}\right) \qquad (2)$$

is performed. Here, N_0 is the concentration of localized states. For the energy scale ε_0 of the band tail in (GaIn)(NAs), a typical value of 10 meV is used [62, 65]. The phonon-assisted exciton hopping rate Γ_{ij} from state i to state j is determined by the Miller–Abrahams expression [67]

$$\Gamma_{ij} = \nu_0 \exp\left(-\frac{2r_{ij}}{\alpha} - \frac{\varepsilon_j - \varepsilon_i + |\varepsilon_j - \varepsilon_i|}{2kT}\right), \qquad (3)$$

where ν_0 is the attempt-to-escape frequency, which is usually of the order of $10^{13}\,\mathrm{s}^{-1}$; r_{ij} is the distance between the localized sites i and j with energies ε_i and ε_j, respectively; α is the localization length; k is Boltzmann's constant; and T is the temperature. We use the following parameters in our calculation: $N_0\alpha^2 = 0.6$ and $\tau_0\nu_0 = 2.0 \times 10^4$ corresponding to the exciton lifetime of $\tau_0 = 2.0$ ns.

Figure 17 (top) shows the calculated photoluminescence spectrum assuming the exponential density of states given in Eq. (2). For low temperatures, excitons hop to their adjacent local minimum before recombining. With rising temperature, they become more mobile and are enabled to find deeper states within a wider distance to their original location, thus red shifting the luminescence. Finally, for temperatures on the order of ε_0/k, the photoluminescence spectrum increasingly mirrors the density of states [66]. In Fig. 17 (bottom) we display the temperature-dependent Stokes shift. The typical S-shape is clearly observable. The observation of the same trends as in experiments [62, 65] indicates that the
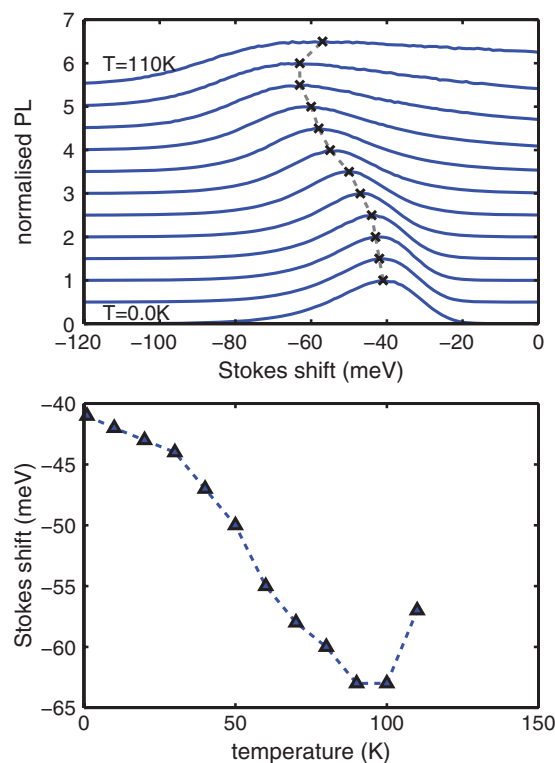

Figure 17 (online color at: www.pss-b.com) Top: Temperature-dependent photoluminescence calculated assuming bound excitons hopping in a disordered environment with an exponential distribution of states. The temperature varies from 0 to 110 K in steps of 10 K. Crosses indicate the maxima of the photoluminescence signal. The dashed line is a guide to the eye. For the calculation, we used the following parameters: $N_0\alpha^2 = 0.6$, $\varepsilon_0 = 10$ meV, and $\tau_0\nu_0 = 2.0 \times 10^4$. Bottom: S-shape in the temperature-dependent Stokes shift. The phenomenon may be observed experimentally in (GaIn)(NAs) [58–62] and serves as an indicator of exciton hopping behavior. The dashed line is a guide to the eye.

low-temperature photoluminescence in (GaIn)(NAs) is dominated by disorder effects.

6 Ga(AsSb)-based emitters at 1.3 μm Ga(AsSb) compounds constitute an alternative to the dilute nitride (GaIn)(NAs) material system in the domain of GaAs-based emitters operating at 1.3 μm. The material has already been used in vertical-cavity surface-emitting laser (VCSEL) systems [68], however, to fully explore the possibilities and to optimize the structural designs, the material system needs to be characterized in detail.

For a long time the band alignment of Ga(AsSb) embedded in GaAs for antimony concentrations of about 35%, which are required to achieve emission at 1.3 μm, has remained an unresolved question. In fact, it was controversially discussed whether the structure is either type-I, where electrons and holes are confined in the Ga(AsSb) layer, or type-II, where electrons and holes are spatially separated in adjacent layers [69, 70]. As our microscopic analysis allows for a detailed analysis of the optical spectra, the controversial discussion on the confinement potential can finally be clarified.

For this purpose we investigate a series of Ga(AsSb)/GaAs/(AlGa)As quantum-well structures by electroabsorption. The samples consist of a 7 nm wide $Ga(As_{0.64}Sb_{0.36})$ single quantum well with GaAs spacers of varying width (0, 1, 2, 3, 6, and 9 nm) on either side which are in turn placed within $(Al_{0.25}Ga_{0.75})As$ barrier layers [71]. In Section 5.1, we discuss the suitability of photomodulated reflectance investigations for the characterization of quantum-well structures; here we employ the electroabsorption method which is an adequate modulation technique as well. Experimentally, a square wave voltage is applied to the sample while the field-induced change in absorption is measured [72]. In order to analyze and interpret the resulting spectra which are nontrivial in general, we calculate absorption spectra for two different electric fields applied in growth directions. Subtracting these two spectra from each other yields the electroabsorption signal. Due to the field-induced change of the oscillator strength, higher-order quantum-well transitions are also sensitively revealed (Fig. 18, top). Hence, the modulation technique is especially useful for the characterization of critical structural parameters.

The microscopic simulations demonstrate that the conduction band offset between Ga(AsSb) and GaAs is the most sensitive parameter for the line shape. Through the comparison of calculated spectra for different offset situations with experimental data we can conclude a spatially indirect confinement potential with a conduction band offset of 40 ± 20 meV (Fig. 18, bottom). In that case, the line shapes of both the first and the second resonance (around 1.04 and 1.12 eV, respectively) are quite well reproduced, and their spectral distance matches the experiment. The conclusion is verified by the investigation of electroabsorption spectra for different external electric fields and for further samples [73, 74].
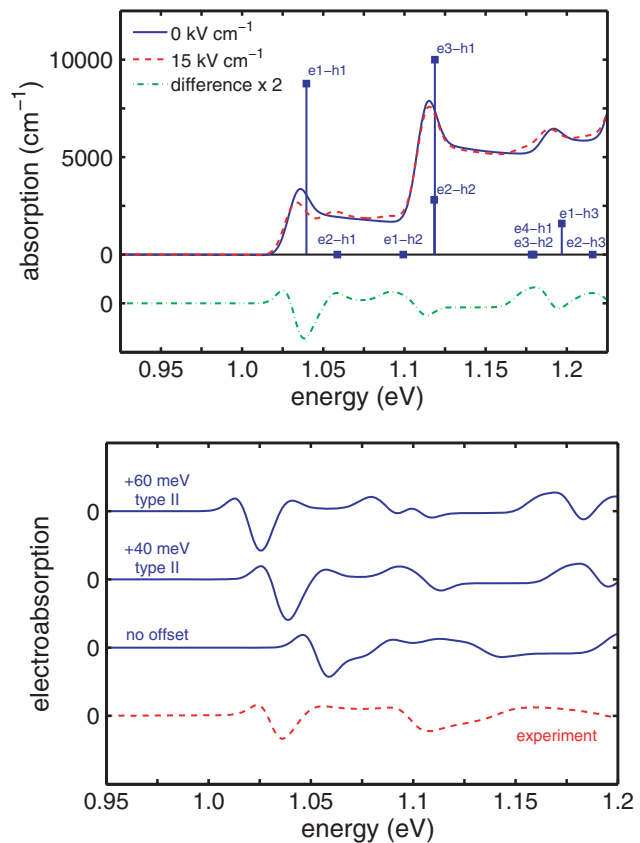

Figure 18 (online color at: www.pss-b.com) Top: Calculated absorption spectra for the 7 nm wide $Ga(As_{0.64}Sb_{0.36})$ quantum well with 6 nm wide GaAs spacers on both sides surrounded by $(Al_{0.25}Ga_{0.75})As$ barriers in the field-free case (solid line) and for an electric field of 15 kV cm^{-1} (dashed line) at a temperature of 30 K. The bars indicate the optical strength of the various interband transitions. The electroabsorption spectrum is obtained by calculating the difference between the two absorption spectra (dash-dotted line) and is vertically shifted for clarity. Bottom: Comparison of experimental (dashed line) and theoretical (solid lines) electroabsorption spectra. The calculations are for different band offset situations and are vertically displaced. Obviously, the best agreement between experiment and theory is achieved for the 40 meV type-II offset, which means a spatially indirect confinement potential. The experiment was done by G. Blume, P. J. Klar, and G. Weiser at the Philipps-University Marburg [73].

7 Nonequilibrium effects The characterization of active materials and in particular the VECSEL properties presented in the previous sections result from a stationary laser description with a quasi-equilibrium gain medium approach. However, the assumption of quasi-equilibrium carrier distributions disregards the effects of spectral hole burning and, in the case of optically in-well pumped devices, the bleaching of the absorption due to pump-induced blocking. Additionally, the effect of an enhanced carrier temperature compared to the lattice system is often neglected. Both, the nonequilibrium carrier distribution and the elevated carrier temperature, cause higher latent carrier density and thus reduce the laser efficiency.

Feature
Article

Phys. Status Solidi B **247**, No. 4 (2010)   803

Moreover, the active mirror heats up too, causing the so-called thermal rollover [5, 75–77].

To address nonequilibrium aspects, we could use the full semiconductor Bloch equations. However, since this requires excessive numerical calculations, we often resort to a systematically simplified approach. To separate the impact of the nonequilibrium carrier distributions from the heating effects of the mirror, we assume optimal heat conductivity to the external heatsink. Thus, the lattice temperature of the active material is kept constant. Dynamical temperature changes involve additional solutions of the heat-conduction equations, which are numerically feasible but excluded here for simplicity.

As already introduced and used in the previous sections, the description of the dynamic response of the laser device is performed in terms of equations of motion for the quantum-well polarization. However, in order to monitor the correct carrier distributions resulting from the continuous generation and recombination of carriers in the laser, additional microscopic equations of motion for the carriers have to be solved self-consistently with the polarization equations. The higher order Coulomb correlations occurring in the equations can be treated microscopically yielding the precise dynamics of carrier creation and scattering [8]. This scattering is of an elementary nature for the description of the nonequilibrium carrier dynamics since the pump energy has to be higher than the laser energy. Thus, carriers injected with high pump energy $\hbar\omega_{pump}$ in the band have to scatter down to the band minimum where they can recombine stimulatingly.

The drawback of the rigorous scattering treatment [8] is the needed numerical effort resulting in very long calculation times for the accurate laser dynamics. As a short cut, we developed a scattering-rate approach [78] with structural, temperature, density, and pump-energy-dependent scattering rates. We use this method in combination with a dephasing time approach for the polarization, yielding sufficiently fast numerics for the laser simulation. We have to underline at this point, that the predictivity of this model crucially relies on the correct scattering and dephasing times, which therefore have to be calculated separately with the full microscopic theory. The carrier losses due to spontaneous emission and Auger processes are calculated via the microscopic theory already introduced in Section 2. Hence, the scattering-rate model preserves the microscopic nature of our approach but sacrifices the full self-consistency in order to allow for significant reductions in computation time.

The model system under investigation is an (InGa)As-based VECSEL with a design wavelength of $\lambda_{laser} = 1045$ nm. We assume an active region consisting of 14 (In$_{0.21}$Ga$_{0.79}$)As quantum wells with 8 nm thickness grown on a 26.5 double layer GaAs/AlAs Bragg mirror. The wells are arranged in a resonant periodic gain configuration with (Al$_{0.06}$Ga$_{0.94}$)As barriers. An (AlGa)As cap layer finishes the active mirror which is then arranged with the external outcoupling mirror in a linear resonator geometry. For the calculations, an external mirror reflectivity of 98% is assumed.

The computed equilibrium absorption spectrum of the active material is shown in Fig. 19 for different carrier
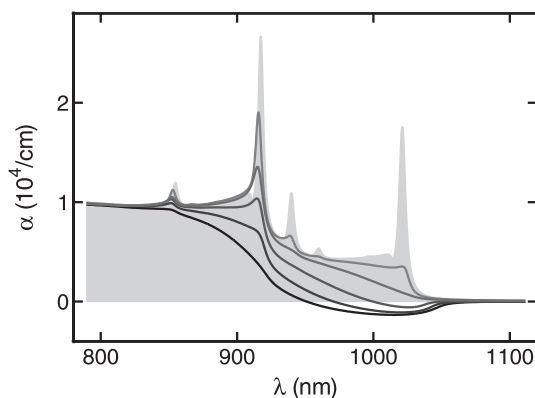
Figure 19 Quantum-well-absorption spectra calculated with the semiconductor Bloch equations for different equilibrium carrier distributions and a carrier temperature of 305 K. The plotted densities are (from gray to black): 5×10^{11} cm^{-2}, 1×10^{12} cm^{-2}, 2×10^{12} cm^{-2}, 3×10^{12} cm^{-2}, and 4×10^{12} cm^{-2}. The shaded area indicates the linear absorption of the quantum well.

densities. Here, two conduction and five valence bands have to be taken into account to cover the spectral range from the quantum-well-band gap to the fundamental gap of the barrier (i.e., 1.55 eV). The shaded area in Fig. 19 is the linear absorption spectrum with clear excitonic signatures of the dipole transitions between the different bands under consideration. For higher densities, starting from 5×10^{11} cm^{-2} (dark gray) to 4×10^{12} cm^{-2} (black), the excitonic signatures wash out and reveal gain in the vicinity of the bandgap for sufficient large carrier density.

Our calculations show that carrier densities around 2×10^{12} cm^{-2} are necessary for laser operation. Here, a strong wavelength dependence of the quantum-well absorption is visible, especially a strong reduction of absorption below 915 nm due to the Pauli blocking of the resident carriers (cf. Section 3.4).

The description of the laser is completed by a wave equation for the electrical field in the cavity. Together with the semiconductor Bloch equations, we get the Maxwell-Semiconductor Bloch Equations (MSBE), which allow for the modeling of the coupled electronic and optical features of the laser [79]. In the description of the pump field, we neglect the spectrally dependent reflection of the dielectric structure to directly monitor the impact of the nonequilibrium on the power characteristics. However, including these effects would just alter the pump-absorption efficiency to a product with this reflectivity (cf. the discussion of Section 3.4).

7.1 Optical in-well pumping In addition to the discussion in Section 3, the strong wavelength dependence of the quantum-well absorption plays a crucial role for the choice of the optimal pump wavelength λ_{pump} for high-power application. On the one hand side, a low pump energy is desirable, due to the dependence of the internal conversion efficiency of the VECSEL on the quantum defect $\eta_{QD} = \lambda_{pump}/\lambda_{laser}$ [7]. A high internal efficiency means low thermal losses and therefore less heat generation leading

to, in principle, higher possible output powers. On the other hand, the absorption efficiency η_{abs} drops with reduced pump energy as depicted in Fig. 19. Thus, the total efficiency $\eta = \eta_{abs}\eta_{QD}\eta_{out}$ with the outcoupling efficiency $\eta_{out} = \ln R_2 / \ln R_1 R_2 T_{loss}$ [7] of the device is reduced. Here, R_1, R_2 are the reflectivities of the Bragg and external mirror, and $1 - T_{loss}$ the optical round trip transmission loss in the device. For high-power applications, this drawback of reduced pump absorption can be compensated by more complicated pump geometries, i.e., a recycling of the reflected pump light (e.g., see Ref. [22]).

The calculated steady state VECSEL emission intensity of the quantum-well-pumped device is shown in Fig. 20a for incident pump intensities of 280, 437, and 984 kW cm^{-2}. Here, the wavelength dependence of the absorption spectrum (Fig. 19) is resembled as anticipated: for a pump wavelength below 920 nm, the emitted intensity shows only a weak dependence on the actual pump wavelength. Above 920 nm, the pump-absorption drops due to the phase space filling. Hence, the creation of carriers due to the pump and thus the emission is reduced.

Corresponding to the emission intensity, the carrier temperatures and the steady-state carrier density show a strong wavelength dependence, as shown in Fig. 20b. The carrier temperatures are defined as the temperatures of the Fermi-Dirac distributions of the scattering-rate approach and thus are a measure of the mean energy of the particles in the corresponding bands. As depicted in Fig. 20b, the carrier temperatures of electrons and holes deviate from each other. This is a consequence of the particular band structure. The plasma temperature T_{plasma}, plotted as the solid black line in Fig. 20b, is the mean temperature of all carriers in the quantum well. As already stated before, T_{plasma} exceeds the lattice temperature, which we set to 305 K, for all pump intensities. The increased carrier temperature is strongly influenced by the quantum defect which provides the largest fraction of the total dissipated heat. Consequently, the temperatures basically follow the laser emission of Fig. 20a, leading to smeared out Fermi-Dirac distributions. This anticipates that the observed increase of the carrier density Fig. 20b (gray line) is a consequence of the carrier temperatures.

The optical pump and the laser emission introduce nonequilibrium effects in the actual shape of the carrier occupations leading to deviations from a Fermi-Dirac distribution. With the MSBE, the full microscopic carrier distributions under lasing conditions are accessible. However, one often is not interested in the complete nonequilibrium carrier distribution but likes to have a measurement how "nonequilibrium" the actual carrier distribution is. Therefore, we introduce a quantity

$$\text{NEq} = \frac{1}{2} \frac{\int |n_\nu(k) - f_\nu(k)| k \, dk}{\int n_\nu(k) k \, dk}, \tag{4}$$

such that NEq is a measure of the relative portion of all carriers in the NEq carrier distribution; $n_\nu(k)$ in band ν which
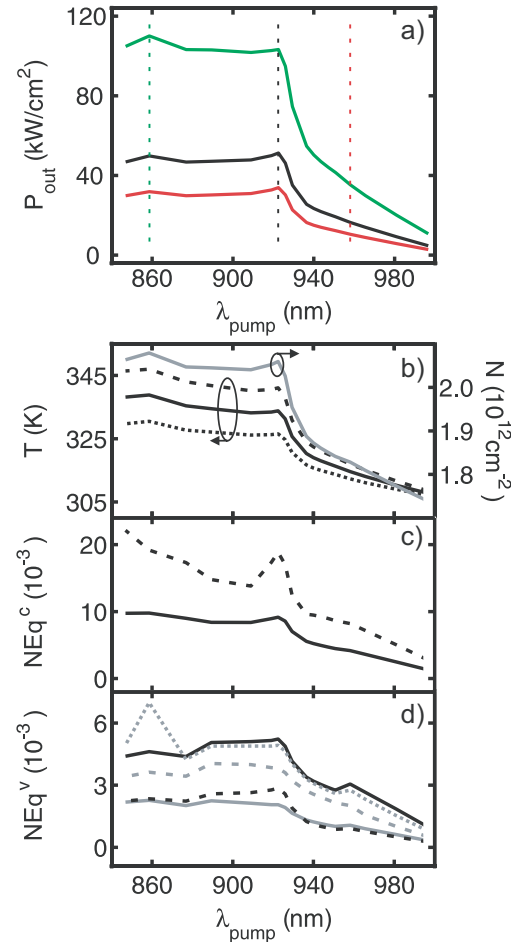

Figure 20 (online color at: www.pss-b.com) Steady state VECSEL emission intensity (a), carrier temperatures and densities (b), and nonequilibrium measure *NGG* (c and d). The emission intensity in subplot (a) is shown for $P_{pump} = 280\,\text{kW cm}^{-2}$ (red line), $437\,\text{kW cm}^{-2}$ (black line), and $984\,\text{kW cm}^{-2}$ (green line), the data in the subplots (b–d) for $P_{pump} = 437\,\text{kW cm}^{-2}$. In subplot (b), the plasma temperature T_{plasma} (black solid line), the hole temperature T^h (black dotted line), the electron temperature T^e (black dashed line), and the carrier density (gray solid line) are shown. Subplot (c) shows the nonequilibrium measure NEq for the two conduction bands (c1: black solid line; c2: black dashed line) and subplot (d) for the five valence bands (v1: black solid line; v2: black dashed line; v3: gray solid line; v4: gray dashed line; and v5: gray dotted line).

deviate from the Fermi-Dirac distribution $f_\nu(k)$ at temperature $T^{e,h}$ of that band.

In subplots (c and d) of Fig. 20, the quantity NEq is plotted for both conduction bands (c) and for the five valence bands (d), revealing that up to 2% of the carriers are in states that would not be populated with the statistic distribution. Again, the examined quantity follows roughly the dependence of the output intensity with respect to the pump energy. However, differences in NEq between the band types on the one hand and the subband index on the other hand are visible. This is a result of the particular dipole matrix elements for

the band to band transitions and the particular subband structure.

The deviations of the carrier distributions from the statistical shape are such that the occupation probability around $k = 0$ is reduced due to the stimulated recombination of carriers. This is called kinetic hole burning. For in-well pumped systems, the carrier occupation for momenta corresponding to the pump wavelength is increased. The latter effect causes an additional reduction of the pump absorption while the spectral hole burning reduces the material gain. The gain reduction is then compensated by an increase in the overall carrier density.

The resulting power characteristics for the pump wavelengths of 958, 923, and 859 nm (dashed lines in Fig. 20a) are shown in Fig. 21a. Here, a clearly sublinear dependence between pump and emission can be observed for all wavelengths. This can be nicely seen in the comparison with the equilibrium power characteristic, where $T_{carr} = T_{latt}$. The latter one is shown exemplarily in Fig. 21a for $\lambda_{pump} = 923$ nm as shaded line. The observed deviations in the slope efficiencies for the different pump wavelengths are a consequence of the spectral dependence of the pump absorption.
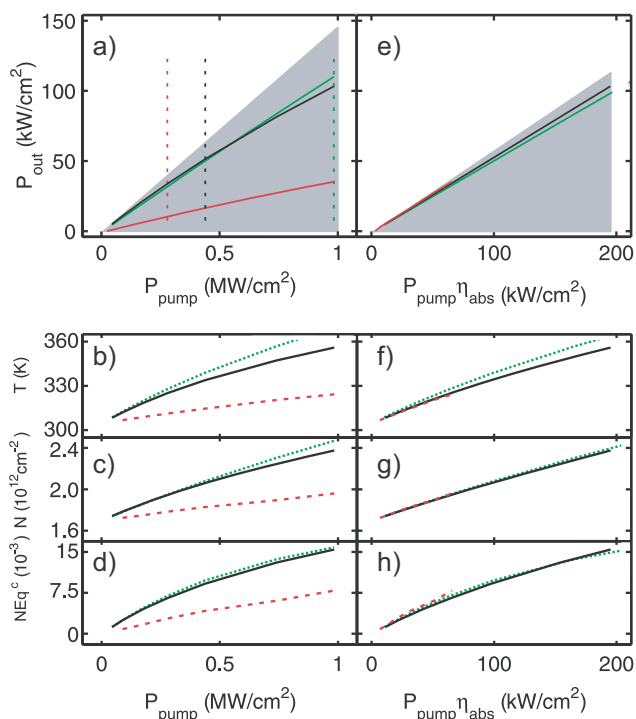

Figure 21 (online color at: www.pss-b.com) Power characteristic (a and e), plasma temperature (b and f), carrier density (c and g), and NEq (d and h) for quantum-well-pumped VECSEL with $\lambda_{pump} = 859$ nm (green line), 923 nm (black line), and 958 nm (red line). The left column (a–d) is plotted *versus* the incident pump power, the right column (e–h) *versus* the absorbed pump power. In (a and e), the power characteristics for equilibrium carrier distributions with $T_{plasma} = T_{lattice}$ for $\lambda_{pump} = 923$ nm are shown for comparison (shaded areas).

Subplots (b–d) present the corresponding plasma temperature, carrier density, and NEq for the first conduction band. In analogy to the wavelength considerations of Fig. 20, the characteristics of the temperature, density, and NEq follow the laser emission. To separate the nonequilibrium effects on the carrier density causing higher threshold losses from the modified pump absorption, we plot in subplots (e–h) the same quantities as in (a–d) as functions of the absorbed pump intensity. Here, the observed sublinearity of the power characteristics is suppressed and the different slope efficiencies virtually vanishes. From this, we conclude, that the primary effect of the elevated carrier temperatures and the nonequilibrium carrier distributions is a reduction of the pump absorption. Nevertheless, both, temperature increase and nonequilibrium, leads to a density increase which is followed by an increase of the carrier losses and thus results in the remaining sublinearity in Fig. 21e. This is supported by the carrier density in subplot (g) being less sublinear than the temperature increase in (f).

7.2 Optical barrier pumping To complete our pumping analysis, we apply a barrier pumping scheme to the same VECSEL device. Therefore, the theoretical description has to be extended to the three-dimensional barrier system, which is described by two additional bands in parabolic approximation and a bandgap of $\hbar\omega_{barrier} = 1.517$ eV or $\lambda_{barrier} = 817$ nm. The scattering of excited carriers into the wells is modeled by another scattering rate, which we set to 2 ps in agreement with the published data range [80–82]. Due to the fact, that the barrier absorption is less energy dependent, we set λ_{pump} to a constant value of 800 nm. The relatively large barrier width leads to a high absolute absorption. Therefore, the absorbed intensity approximates the incident intensity, i.e., $\eta_{abs} \approx 1$.

Figure 22a shows the resulting power characteristic. Here, only very slight deviations from the equilibrium result, indicated by the shaded area, are visible. This is due to the low carrier density in the barriers, leading to a vanishing Pauli blocking of the pump absorption. In subplot (b), the corresponding quantum-well-carrier density (solid line) and the medium sheet density of the three-dimensional barrier density (dashed line) are shown. As in the in-well pumping, the carrier density increases with pump intensity due to the increase of the carrier temperature, as a consequence of the quantum defect. This temperature dependence is shown in subplot (c) as a gray line, displaying the expected higher deviations from the constant lattice temperature than in the in-well pumping case. The black line in (c) corresponds to the NEq value for the first conduction band. This value is lower in amplitude than the corresponding in-well quantity due to the absence of a pump peak in the quantum-well-carrier distributions.

All in all, quantum-well-pumped VECSEL can be expected to show prominent nonequilibrium features which lead to reduced gain amplitudes. As a consequence, one needs stronger pumping to increase the carrier densities which in turn reduces the pump absorption due to Pauli
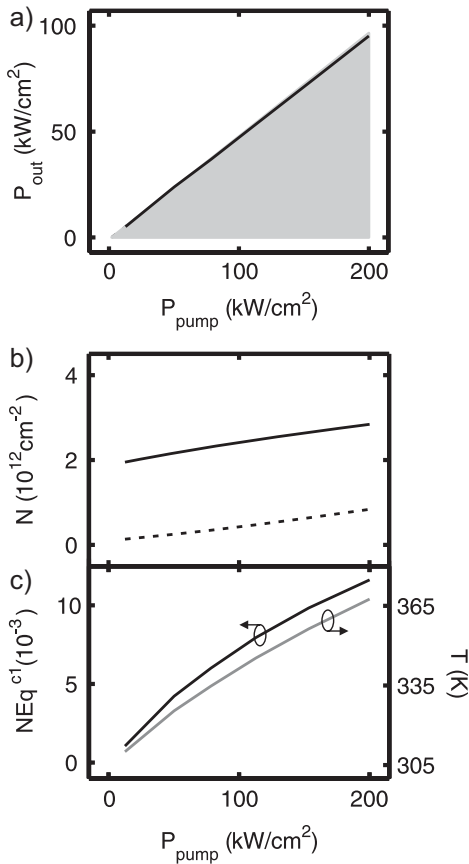
Figure 22 Power characteristics (a), carrier density (b), temperature and NEq (c) of the barrier pumped system. The shaded area in (a) depicts the equilibrium result, while the solid line corresponds to the full calculation. In (b) the quantum-well-carrier density (solid line) and the medium barrier sheet density (dashed line) is plotted. Subplot (c) shows the plasma temperature T_{plasma} (gray line) and the NEq (black line).

blocking. Consequently, η_{abs} drops and P_{th} increases leading to a sublinear power characteristics even for the ideal case of constant lattice temperature. The comparison of the in-well pumped device with the barrier pumped VECSEL shows that NEq is less pronounced due to the additional scattering mechanisms in the barriers while carrier temperature and density rise in comparison to the in-well case. The resulting sublinear power characteristic shows only minor deviations from the equilibrium calculation.

8 Conclusions In conclusion, a microscopic many-particle model is evaluated for various gain media used in semiconductor laser devices. The theory allows us to quantitatively calculate optical material properties such as absorption, gain, luminescence, as well as the intrinsic laser loss processes which critically influence the performance of a laser system. The microscopic results can be integrated into laser device simulations. On the one hand, the theory is used to analyze spectroscopic measurements offering an accurate method to characterize specific semiconductor structures and on the other hand, lasing properties may be evaluated including threshold behavior or power characteristics. In this manner, novel material systems and structures can be studied systematically to explore their application potential and to design optimized semiconductor laser devices.

References

[1] A. C. Tropper, H. D. Foreman, A. Garnache, K. G. Wilcox, and S. H. Hoogland, J. Phys. D **37**, R75 (2004).
[2] A. C. Tropper and S. Hoogland, Prog. Quantum Electron. **30**, 1 (2006).
[3] U. Keller and A. C. Tropper, Phys. Rep. **429**, 67 (2006).
[4] N. Schulz, J.-M. Hopkins, M. Rattunde, D. Burns, and J. Wagner, Laser Photon. Rev. **2**, 160 (2008).
[5] S. Calvez, J. E. Hastie, M. Guina, O. G. Okhotnikov, and M. D. Dawson, Laser Photon. Rev. **3**, 407 (2009).
[6] M. Kuznetsov, F. Hakimi, R. Sprague, and A. Mooradian, IEEE Photon. Techn. Lett. **9**, 1063 (1997).
[7] M. Kuznetsov, F. Hakimi, R. Sprague, and A. Mooradian, IEEE J. Sel. Top. Quantum Electron. **5**, 561 (1999).
[8] J. Hader, S. W. Koch, and J. V. Moloney, Solid-State Electron. **47**, 513 (2003).
[9] J. Hader, J. V. Moloney, and S. W. Koch, IEEE J. Quantum Electron. **41**, 1217 (2005).
[10] J. Hader, J. V. Moloney, M. Fallahi, L. Fan, and S. W. Koch, Opt. Lett. **31**, 3300 (2006).
[11] J. Hader, J. V. Moloney, and S. W. Koch, Appl. Phys. Lett. **89**, 171120 (2006).
[12] C. Bückers, A. Thränhardt, S. W. Koch, M. Rattunde, N. Schulz, J. Wagner, J. Hader, and J. V. Moloney, Appl. Phys. Lett. **92**, 071107 (2008).
[13] W. W. Chow and S. W. Koch, Semiconductor – Laser Fundamentals (Springer, Berlin, 1999).
[14] O. Madelung (ed.), Semiconductors – Basic Data, second edition (Springer, Berlin, 1996).
[15] I. Vurgaftman, J. R. Meyer, and L. R. Ram-Mohan, J. Appl. Phys. **89**, 5815 (2001).
[16] H. Haug and S. W. Koch, Quantum Theory of the Optical and Electronic Properties of Semiconductors, fourth edition (World Scientific, Singapore, 2004).
[17] A. Girndt, F. Jahnke, A. Knorr, S. W. Koch, and W. W. Chow, Phys. Status Solidi B **202**, 725 (1997).
[18] J. Hader, J. V. Moloney, S. W. Koch, and W. W. Chow, IEEE J. Sel. Top. Quantum Electron. **9**, 688 (2003).
[19] M. Kira, F. Jahnke, W. Hoyer, and S. W. Koch, Prog. Quantum Electron. **23**, 189 (1999).

Phys. Status Solidi B **247**, No. 4 (2010)

807

[20] M. Schafer, W. Hoyer, M. Kira, S. W. Koch, and J. V. Moloney, J. Opt. Soc. Am. B **25**, 187 (2008).

[21] J. Hader, J. V. Moloney, B. Pasenow, S. W. Koch, M. Sabathil, N. Linder, and S. Lutgen, Appl. Phys. Lett. **92**, 261103 (2008).

[22] W. Zhang, T. Ackemann, S. McGinily, M. Schmid, E. Riis, and A. I. Ferguson, Appl. Opt. **45**, 7729 (2006).

[23] S. J. McGinily, R. H. Abram, K. S. Gardner, E. Riis, A. I. Ferguson, and J. S. Roberts, IEEE J. Quantum Electron. **43**, 445 (2007).

[24] C. Bückers, S. Imhof, A. Thränhardt, J. Hader, J. V. Moloney, and S. W. Koch, IEEE J. Sel. Top. Quantum Electron. **15**, 984 (2009).

[25] J. E. Hastie, J.-M. Hopkins, S. Calvez, C. W. Jeon, D. Burns, R. Abram, E. Riies, A. I. Ferguson, and M. D. Dawson, IEEE Photon. Techn. Lett. **15**, 894 (2003).

[26] M. Schmid, S. Benchabane, F. Torabi-Goudarzi, R. Abram, A. I. Ferguson, and E. Riies, Appl. Phys. Lett. **84**, 4860 (2004).

[27] G. D. Clark and N. Holonyak, Phys. Rev. **156**, 913 (1967).

[28] S. Gehrsitz, F. K. Reinhart, C. Gourgon, N. Herres, A. Vonlanthen, and H. Sigg, J. Appl. Phys. **87**, 7825 (2000).

[29] A. J. Kemp, G. J. Valentine, J.-M. Hopkins, J. E. Hastie, S. A. Smith, S. Calvez, M. D. Dawson, and D. Burns, IEEE J. Quantum Electron. **41**, 148 (2005).

[30] J. G. Kim, L. Shterengas, R. U. Martinelli, G. L. Belenky, D. Z. Garbuzov, and W. K. Chan, J. Appl. Phys. **81**, 3146 (2002).

[31] E. A. Pease, L. R. Dawson, L. G. Vaughn, P. Rotella, and L. F. Lester, J. Appl. Phys. **93**, 3177 (2003).

[32] M. Rattunde, J. Schmitz, G. Kaufel, M. Kelemen, J. Weber, and J. Wagner, Appl. Phys. Lett. **88**, 081115 (2006).

[33] N. Schulz, M. Rattunde, C. Manz, K. Köhler, C. Wild, J. Wagner, S.-S. Beyertt, U. Brauch, T. Kübler, and A. Giessen, IEEE Photon. Techn. Lett. **18**, 1070 (2006).

[34] M. Rattunde, M. T. Kelemen, N. Schulz, C. Pfahler, C. Manz, J. Schmitz, G. Kaufel, and J. Wagner, High-Brightness 2.X µm Semiconductor Lasers, in: Mid-infrared Coherent Sources and Applications, edited by M. Ebrahimzadeh, and I. Sorokina (Springer, Dordrecht, 2007).

[35] N. Schulz, B. Rösener, R. Moser, M. Rattunde, C. Manz, K. Köhler, and J. Wagner, Appl. Phys. Lett. **93**, 181113 (2008).

[36] J. R. Meyer, C. A. Hoffmann, F. J. Bartoli, and L. R. Ram-Mohan, Appl. Phys. Lett. **67**, 757 (1995).

[37] J. Faist, F. Capasso, D. L. Sivco, C. Sirtori, A. L. Hutchinson, and A. Y. Cho, Science **264**, 553 (1994).

[38] J. Hader, J. V. Moloney, S. W. Koch, I. Vurgaftman, and J. R. Meyer, Appl. Phys. Lett. **94**, 061106 (2009).

[39] C. L. Candey, W. W. Bewley, J. R. Lindle, C. S. Kim, M. Kim, I. Vurgaftman, and J. R. Meyer, J. Electron. Mater. **35**, 453 (2006).

[40] M. Weyers, M. Sato, and H. Ando, Jpn. J. Appl. Phys. **31**, 853 (1992).

[41] E. P. O'Reilly and A. Lindsay, Phys. Status Solidi B **216**, 131 (1999).

[42] A. Lindsay and E. P. O'Reilly, Solid State Commun. **112**, 443 (1999).

[43] Band Structure Parameters are from: Landolt-Börnstein, Vol. 41A1, edited by O. Madelung, U. Rössler, and M. Schulz (Springer, Berlin, 2001/2002); and W. W. Chow and S. W. Koch, Semiconductor-Laser Fundamentals (Springer, Berlin, 1999). The nitrogen influence on the gap energy was derived from comparisons to experiment. For the band alignment, 36% of the gap difference $\Delta_{layer} = E_{g,GaAs} - E_{g,layer}$ are attributed to the valence band and 64% to the conduction band. In case of Ga(NAs), an offset component x V_{off}, $V_{off} = 1.5$ eV, is added to the valence band to account for the influence of the anticrossing.

[44] E. Y. Wang, W. A. Albers, Jr. and C. E. Bleil, Light-modulated Reflectance of Semiconductors, in: II–VI Semiconducting Compounds, 1967 International Conference, edited by D. G. Thomas (W.A. Benjamin, Inc., New York, 1967).

[45] R. E. Nahory and J. L. Shay, Phys. Rev. Lett. **21**, 1569 (1968).

[46] J. Misiewicz, P. Sitarek, G. Sek, and R. Kudrawiec, Mater. Sci. (Pol) **21**, 263 (2003).

[47] C. Schlichenmaier, H. Grüning, A. Thränhardt, P. J. Klar, B. Kunert, K. Volz, W. Stolz, W. Heimbrodt, T. Meier, S. W. Koch, J. Hader, and J. V. Moloney, Appl. Phys. Lett. **86**, 081903 (2005).

[48] A. Thränhardt, I. Kuznetsova, C. Schlichenmaier, S. W. Koch, L. Shterengas, G. Belenky, J.-Y. Yeh, L. J. Mawst, N. Tansu, J. Hader, J. V. Moloney, and W. W. Chow, Appl. Phys. Lett. **86**, 201117 (2005).

[49] K. Hantke, J. D. Heber, C. Schlichenmaier, A. Thränhardt, T. Meier, B. Kunert, K. Volz, W. Stolz, S. W. Koch, and W. W. Rühle, Phys. Rev. B **71**, 165320 (2005).

[50] G. Jaschke, R. Averbeck, L. Geelhaar, and H. Riechert, J. Cryst. Growth **278**, 224 (2005).

[51] S. R. Bank, H. Bae, L. L. Goddard, H. B. Yuen, M. A. Wistey, R. Kudrawiec, and J. S. Harris, IEEE J. Quantum Electron. **43**, 773 (2007).

[52] X. Yang, M. J. Jurkovic, J. B. Heroux, and W. I. Wang, Appl. Phys. Lett. **75**, 178 (1999).

[53] H. Shimizu, K. Kumada, S. Uchiyama, and A. Kasukawa, Electron. Lett. **36**, 1379 (2000).

[54] J. Massies and N. Grandjean, Phys. Rev. B **48**, 8502 (1993).

[55] E. Tournié, N. Grandjean, A. Trampert, J. Massies, and K. H. Ploog, J. Cryst. Growth **150**, 460 (1995).

[56] C. Schlichenmaier, A. Thränhardt, T. Meier, S. W. Koch, W. W. Chow, J. Hader, and J. V. Moloney, Appl. Phys. Lett. **87**, 261109 (2005).

[57] R. Fehse, S. Tomic, A. R. Adams, S. J. Sweeney, E. P. O'Reilly, A. Andreev, and H. Riechert, IEEE J. Sel. Top. Quantum Electron. **8**, 801 (2002).

[58] L. Grenouillet, C. Bru-Chevallier, G. Guillot, P. Gilet, P. Duvaut, C. Vannuffel, A. Million, and A. Chenevas-Paule, Appl. Phys. Lett. **76**, 2241 (2000).

[59] M.-A. Pinault and E. Tournié, Appl. Phys. Lett. **78**, 1562 (2001).

[60] I. A. Buyanova, W. M. Chen, and C. W. Tu, Semicond. Sci. Technol. **17**, 815 (2002).

[61] A. Hierro, J.-M. Ulloa, J.-M. Chauveau, A. Trampert, M.-A. Pinault, E. Tournié, A. Guzmán, J. L. Sánchez-Rojas, and E. Calleja, J. Appl. Phys. **94**, 2319 (2003).

[62] H. Grüning, K. Kohary, S. D. Baranovskii, O. Rubel, P. J. Klar, A. Ramakrishnan, G. Ebbinghaus, P. Thomas, W. Heimbrodt, W. Stolz, and W. W. Rühle, Phys. Status Solidi C **1**, 109 (2004).

[63] M. S. Skolnick, P. R. Tapster, S. J. Bass, A. D. Pitt, N. Apsley, and S. P. Aldred, Semicond. Sci. Technol. **1**, 29 (1986).

[64] S. T. Davey, E. G. Scott, B. Wakefield, and G. J. Davies, Semicond. Sci. Technol. **3**, 365 (1988).

[65] O. Rubel, M. Galluppi, S. D. Baranovskii, K. Volz, L. Geelhaar, H. Riechert, P. Thomas, and W. Stolz, J. Appl. Phys. **98**, 063518 (2005).

[66] S. D. Baranovskii, R. Eichmann, and P. Thomas, Phys. Rev. B **58**, 13081 (1998).

[67] A. Miller and E. Abrahams, Phys. Rev. **120**, 745 (1960).

[68] P. Dowd, S. R. Johnson, S. A. Feld, M. Adamcyk, S. A. Chaparro, J. Joseph, K. Hilgers, M. P. Horning, K. Shiralagi, and Y.-H. Zhang, Electron. Lett. **39**, 987 (2003).

[69] A. D. Prins, D. J. Dunstan, J. D. Lambkin, E. P. O'Reilly, A. R. Adams, R. Pritchard, W. S. Truscott, and K. E. Singer, Phys. Rev. B **47**, 2191 (1993).

[70] G. Blume, T. J. C. Hosea, and S. J. Sweeney, Phys. Status Solidi A **202**, 1244 (2005).

[71] S. R. Johnson, C. Z. Guo, S. Chaparro, Yu, G. Sadofyev, J. Wang, Y. Cao, N. Samal, J. Xu, S. Q. Yu, D. Ding, and Y.-H. Zhang, J. Cryst. Growth **251**, 521 (2003).

[72] K. Satzke, H. G. Vestner, G. Weiser, L. Goldstein, and A. Perales, J. Appl. Phys. **69**, 7703 (1991).

[73] C. Bückers, G. Blume, A. Thränhardt, C. Schlichenmaier, P. J. Klar, G. Weiser, S. W. Koch, J. Hader, J. V. Moloney, T. J. C. Hosea, S. J. Sweeney, J.-B. Wang, S. R. Johnson, and Y.-H. Zhang, J. Appl. Phys. **101**, 033118 (2007).

[74] A. Thränhardt, C. Bückers, C. Schlichenmaier, I. Kuznetsova, S. W. Koch, J. Hader, and J. V. Moloney, Opt. Quantum Electron. **38**, 1005 (2006).

[75] A. R. Zakharian, J. Hader, J. V. Moloney, S. W. Koch, P. Brick, and S. Lutgen, Appl. Phys. Lett. **83**, 1313 (2003).

[76] J. V. Moloney, J. Hader, and S. W. Koch, Laser Photon. Rev. **1**, 24 (2007).

[77] E. Kühn, A. Thränhardt, C. Bückers, S. W. Koch, J. Hader, and J. V. Moloney, J. Appl. Phys. **106**, 063105 (2009).

[78] A. Thränhardt, S. Becker, C. Schlichenmaier, I. Kuznetsova, T. Meier, S. W. Koch, J. Hader, J. V. Moloney, and W. W. Chow, Appl. Phys. Lett. **85**, 5526 (2004).

[79] W. W. Chow, H. C. Schneider, S. W. Koch, C.-H. Chang, L. Chrostowski, and C. Chang-Hasnain, IEEE J. Quantum Electron. **38**, 402 (2002).

[80] J. Hader, J. V. Moloney, and S. W. Koch, Appl. Phys. Lett. **85**, 369 (2004).

[81] J. Christen, D. Bimberg, A. Steckenborn, and G. Weimann, Appl. Phys. Lett. **44**, 84 (1984).

[82] J. A. Brum, T. Weil, J. Nagle, and B. Vinter, Phys. Rev. B **34**, 2381 (1986).